

**MATERIALS SCIENCE DIVISION
COAL TECHNOLOGY EIGHTH QUARTERLY REPORT,
JULY-SEPTEMBER 1976**

**RETURN TO REFERENCE FILE
TECHNICAL PUBLICATIONS
DEPARTMENT**



U W C-AUA-USERDA

ARGONNE NATIONAL LABORATORY, ARGONNE, ILLINOIS

**Prepared for the U. S. ENERGY RESEARCH
AND DEVELOPMENT ADMINISTRATION
under Contract W-31-109-Eng-38**

The facilities of Argonne National Laboratory are owned by the United States Government. Under the terms of a contract (W-31-109-Eng-38) between the U. S. Energy Research and Development Administration, Argonne Universities Association and The University of Chicago, the University employs the staff and operates the Laboratory in accordance with policies and programs formulated, approved and reviewed by the Association.

MEMBERS OF ARGONNE UNIVERSITIES ASSOCIATION

The University of Arizona	Kansas State University	The Ohio State University
Carnegie-Mellon University	The University of Kansas	Ohio University
Case Western Reserve University	Loyola University	The Pennsylvania State University
The University of Chicago	Marquette University	Purdue University
University of Cincinnati	Michigan State University	Saint Louis University
Illinois Institute of Technology	The University of Michigan	Southern Illinois University
University of Illinois	University of Minnesota	The University of Texas at Austin
Indiana University	University of Missouri	Washington University
Iowa State University	Northwestern University	Wayne State University
The University of Iowa	University of Notre Dame	The University of Wisconsin

NOTICE

This report was prepared as an account of work sponsored by the United States Government. Neither the United States nor the United States Energy Research and Development Administration, nor any of their employees, nor any of their contractors, subcontractors, or their employees, makes any warranty, express or implied, or assumes any legal liability or responsibility for the accuracy, completeness or usefulness of any information, apparatus, product or process disclosed, or represents that its use would not infringe privately-owned rights. Mention of commercial products, their manufacturers, or their suppliers in this publication does not imply or connote approval or disapproval of the product by Argonne National Laboratory or the U. S. Energy Research and Development Administration.

Printed in the United States of America
Available from
National Technical Information Service
U. S. Department of Commerce
5285 Port Royal Road
Springfield, Virginia 22161
Price: Printed Copy \$5.00; Microfiche \$3.00

ANL-76-125

ARGONNE NATIONAL LABORATORY
9700 South Cass Avenue
Argonne, Illinois 60439

MATERIALS SCIENCE DIVISION
COAL TECHNOLOGY EIGHTH QUARTERLY REPORT,
July—September 1976

Persons in Charge:

William A. Ellingson
Project Leader

Richard W. Weeks
Associate Division Director

Previous reports in this series

ANL-76-7	July—September 1975
ANL-76-22	October—December 1975
ANL-76-60	January—March 1976
ANL-76-111	April—June 1976

TABLE OF CONTENTS

	<u>Page</u>
HIGHLIGHTS	viii
Abstract	1
Introduction	1
Task A -- Evaluation of Ceramic Refractories for Slagging Gasifiers .	2
Task B -- Evaluation of Ceramic Coatings for Coal-conversion Plants .	8
Task C -- Nondestructive Testing of Coal-plant Components	8
1. Erosion Detection and Monitoring	8
a. Laboratory Ultrasonic Studies	11
b. In-situ Erosion Detection Using Ultrasonic Techniques .	14
c. Erosion and Hot-spot Detection by Infrared Methods . .	16
2. Refractory-installation Studies	19
a. Acoustic-emission Studies for Control of Refractory Curing	19
b. Future Plans	24
c. Radiography Studies Related to Installation of Refractory Liners	24
(1) Field Radiography	24
Bi-Gas Coal Gasifier	24
Radiographic Procedure	27
Results	30
(2) Future Plans	34
3. Valve Studies	34
a. Acoustic Leak Detection	34
b. Future Plans	44
Task D -- Corrosion Behavior of Materials in Coal-conversion Processes	45
Task F -- Component Performance and Failure Analysis	54
1. Synthane Gasifier Distributor Cone Thermocouple (TE-268) Failures	54
References	59

LIST OF FIGURES

<u>No.</u>	<u>Title</u>	<u>Page</u>
1	Slag Attack Exhibited after Run 2 for (a) High-alumina Sinter-bonded, (b) Magnesia-Chrome and Silicon Carbide Type, (c) Phosphate-bonded Alumina, and (d) Fusion-cast Specimens . . .	4
2	Exposed Surface of Magnesium Zirconate-coated Specimen . . .	10
3	Schematic Diagram of HYGAS High-pressure Cyclone Showing Longitudinal Location of Erosion Mapping Positions . . .	12
4	Schematic Diagram of HYGAS High-pressure Cyclone Showing Azimuthal Location of Erosion Mapping Positions . . .	12
5	Apparent Wall Thickness of Inlet Region of High-pressure Cyclone at Longitudinal Position b . . .	13
6	Apparent Wall Thickness of Solids Outlet Region of High-pressure Cyclone as a Function of Longitudinal Position . . .	13
7	Schematic Diagram of Bi-Gas Coal-conversion System Showing Placement of In-situ Erosion-measurement Locations . . .	15
8	Schematic Representation of Erosion-measurement Positions for Product-gas Transfer Line and Coal-feed Transfer Line Blocked Tees . . .	15
9	Schematic Representation of Erosion-measurement Positions for Bi-Gas Coal-feed Transfer Line . . .	17
10	Block Diagram of In-situ Ultrasonic Erosion-measurement Instrumentation for the Bi-Gas Coal-gasification Pilot Plant . .	18
11	Block Diagram of Instrumentation System Used for Acoustic-emission Studies of Refractory Specimens . . .	20
12	Schematic Diagram of Loading System Used to Characterize Acoustic-emission Signals from Refractories . . .	22
13	Photograph of Mold Used to Prepare Refractory Specimens . . .	23
14	Acoustic-emission Signals Emitted from Refractory Specimens under Load . . .	23
15	Relationship between Acoustic-emission rms Levels and Type I Event Counts as a Function of Refractory Density . . .	25
16	Simplified Schematic of Gasifier Vessel Showing Locations at Which Panoramic Gamma Radiographs Were Generated . . .	26

LIST OF FIGURES (Contd.)

<u>No.</u>	<u>Title</u>	<u>Page</u>
17	Cross Section of Location 2 Obtained 2.78 m from the Top Flange of the Gasifier	26
18	Cross Section of Location 3 Obtained 4.78 m from the Top Flange of the Gasifier	28
19	Cross Section of Location 4 Obtained 9.64 m from the Top Flange of the Gasifier	29
20	Film Placement for Locations 2-4	29
21	Radiograph of Location 2 Showing Mortar Lines	31
22	Schematic of Radiograph at Location 2 Showing Details Observed	31
23	Radiograph of Location 3 Showing Mortar Lines, Cooling Tubes, and Penetrameter	32
24	Schematic of Location 3 Radiograph Showing Details Observed .	32
25	Radiograph of Location 4 Showing Cooling Tubes and Penetrameter	33
26	Schematic of Location 4 Radiograph Showing Details Observed .	33
27	Flow Rate of Dry Air at 22°C (72°F) vs Pressure Differential for a 1/64-in. (0.40 mm) Orifice	39
28	Rms Acoustic Output vs Flow Rate of Dry Air at 22°C (72°F) and Pressure for a 1/64-in. (0.40 mm) Orifice Using a Low-g-level Accelerometer	39
29	Rms Acoustic Output vs Flow Rate of Dry Air at 22°C (72°F) for a 1/64-in. (0.40 mm) Orifice Using a Resonant Acoustic- emission Transducer	40
30	Rms Acoustic Output vs Pressure for the Flow of N ₂ through a 1/16-in. (1.59 mm) Orifice Using a Broadband Acoustic- emission Transducer	42
31	Rms Acoustic Output vs Pressure for the Flow of CO ₂ through a 1/16-in. (1.59 mm) Orifice Using a Resonant Acoustic-emission Transducer	42

LIST OF FIGURES (Contd.)

<u>No.</u>	<u>Title</u>	<u>Page</u>
32	Rms Acoustic Output vs Flow Rate of Dry Air through 1/16- and 1/64-in. (1.59 and 0.40 mm) Orifices Using a Resonant Acoustic-emission Transducer	43
33	Scanning-electron Micrographs of Type 304 Stainless Steel after a 136-h Exposure at 875°C to Gas Environments Identified as a, b, and c in the Thermochemical Diagram . . .	48
34	Scanning-electron Micrographs of Type 310 Stainless Steel after a 136-h Exposure at 875°C to Gas Environments Identified as a, b, and c in the Thermochemical Diagram . . .	49
35	Scanning-electron Micrographs of Inconel X750 after a 136-h Exposure at 875°C to Gas Environments Identified as a, b, and c in the Thermochemical Diagram	50
36	Scanning-electron Micrographs of Inconel 671 after a 25-h Exposure at 750°C to Gas Environments Identified as a and b in the Thermochemical Diagram	53
37	Schematic of Synthane Gasifier	56

LIST OF TABLES

<u>No.</u>	<u>Title</u>	<u>Page</u>
I	Refractories Exposed in Slag-abrasion-corrosion Rig Run 2 . . .	3
II	Slag Composition (wt%) during Run 2	7
III	Wear of Coated Metal Specimens after 100-h Exposure to High-velocity Char at 980°C	9
IV	Results of Bi-Gas Field Examination	35
V	Oxygen and Sulfur Partial Pressures (p_{O_2} and p_{S_2}) and Carbon Activities (a_C) Used in the Experimental Runs	46
VI	Failed Components to be Analyzed in the Coming Quarter	55

MATERIALS SCIENCE DIVISION
COAL TECHNOLOGY EIGHTH QUARTERLY REPORT
JULY-SEPTEMBER 1976

HIGHLIGHTS

Task A -- Evaluation of Ceramic Refractories for Slagging Gasifiers
(D. Stahl)

The analysis of specimens from Run 2, a 500-h test with basic slag, is continuing. Run 3, the second 500-h test with basic slag, was begun. Thermal-gradient measurements across the specimens indicate that the gradient was smaller than would be expected with prototypic hot- and cold-face temperatures. A new furnace bottom segment has been designed that will provide these prototypic temperatures.

Task B -- Evaluation of Ceramic Coatings for Coal-conversion Plants
(D. Stahl)

Wear measurements were performed on the magnesium zirconate-coated metal specimens that survived the 100-h test of hot, high-velocity char particles at Solar, Inc. These coatings were not uniformly thick, but they did resist the corrosive and erosive attack.

Task C -- Nondestructive Testing of Coal-plant Components (W. A. Ellingson, W. J. Shack, G. C. Stanton, N. P. Lapinski, and R. F. Vogt)

The in-situ erosion studies have continued this quarter with the development of a convectively cooled ultrasonic waveguide and an attachment method that permits fastening of the waveguide directly to existing components, and final field arrangements have been made for implementation on the Bi-Gas pilot plant. Acoustic-emission studies for application to installation procedures have shown a distinct correlation between refractory density and the acoustic-emission parameters root-mean-square and acoustic counts per event

for a range of refractory densities. Pre- and postcuring gamma radiography studies have been conducted on the Bi-Gas gasifier vessel and show distinct changes in the mortar in the refractory lining. Valve leak-detection studies have continued and indicate that good correlation exists between the mass flow rate and root-mean-square voltage level for the transducer frequency range 20-200 kHz.

Task D -- Corrosion Behavior of Materials in Coal-conversion Processes
(K. Natesan and O. K. Chopra)

Experimental evaluation of the corrosion behavior of commercial iron- and nickel-base alloys in multicomponent gas mixtures that include CO, CO₂, H₂, CH₄, and H₂S is in progress. Oxygen-sulfur thermochemical diagrams were used as a basis in the selection of complex gas environments for the experimental program. Scanning-electron-microscope photographs of the cross sections of different alloys (Types 304 and 310 stainless steel, Inconel X750, and Inconel 671) after exposure to gas environments with various oxygen, sulfur, and carbon potentials are presented. The results show that the corrosion behavior of the commercial alloys in multicomponent gas environments is complex and fundamental processes such as oxidation, sulfidation, and carburization can occur simultaneously with different advancing reaction fronts.

Task F -- Component Performance and Failure Analysis (S. Danyluk, G. M. Dragel, W. J. Shack, and W. A. Ellingson)

Failure analysis of the Synthane gasifier distributor cone thermocouple sheaths (TE-268) was completed. It is concluded that a corrosive environment, off-process temperatures, sheath fabrication factors, and possible cold work of the sheaths contributed to the failures. Recommendations for use of Type 310 stainless steel as a substitute material and changes in the start-up burner, thermocouple sheath specification, and handling prior to

and after installation are made. Preliminary field data have been collected on nine additional failed components from the HYGAS pilot plant, Morgantown Energy Research Center, and Synthane pilot plant.

MATERIALS SCIENCE DIVISION
COAL TECHNOLOGY EIGHTH QUARTERLY REPORT,
JULY-SEPTEMBER 1976

Abstract

This broad-base materials program, begun in October 1974, includes studies on both ceramic (refractory) and metallic materials. Appropriate laboratory and field experiments are integrated. This quarterly report, for the period July-September 1976, presents the technical accomplishments in Tasks A-D and F.

Introduction

The economical conversion of coal into cleaner and more usable fuels will be facilitated through use of the most durable materials systems. The present report is the eighth quarterly progress report submitted by Argonne National Laboratory to the Fossil Energy Research Division of ERDA under project Number 7106, "Materials Technology for Coal Conversion Processes."

The project includes six tasks: (A) evaluation of ceramic refractories exposed to abrasion-corrosion caused by coal slag encountered in slagging gasifiers, (B) evaluation of ceramic coatings and refractories exposed to erosive environments, (C) development, evaluation, and application of nondestructive testing methods applicable to coal-conversion systems, such as in-situ erosion detection/monitoring, (D) development of analytical models to predict corrosion behavior, e.g., phase transformations, of iron- and nickel-base alloys in gaseous environments, (E) development of analytical models to predict the erosion behavior of materials used in coal-gasification plants, and (F) analysis of failed coal-gasification plant components. Progress in Tasks A-D and F is discussed in the present report.*

*Progress in Task E will be presented in the next quarterly report.

Task A -- Evaluation of Ceramic Refractories for Slagging Gasifiers
(Principal Investigator: D. Stahl)

During this quarter, the analysis of the specimens exposed in the second run, a 500-h test with basic slag, continued and the third run, also a 500-h test with basic slag, was begun. Both runs are conducted under conditions expected in the slagging region of gasifiers: 1500°C at oxygen partial pressures of $\sim 10^{-3}$ Pa (10^{-8} atm).

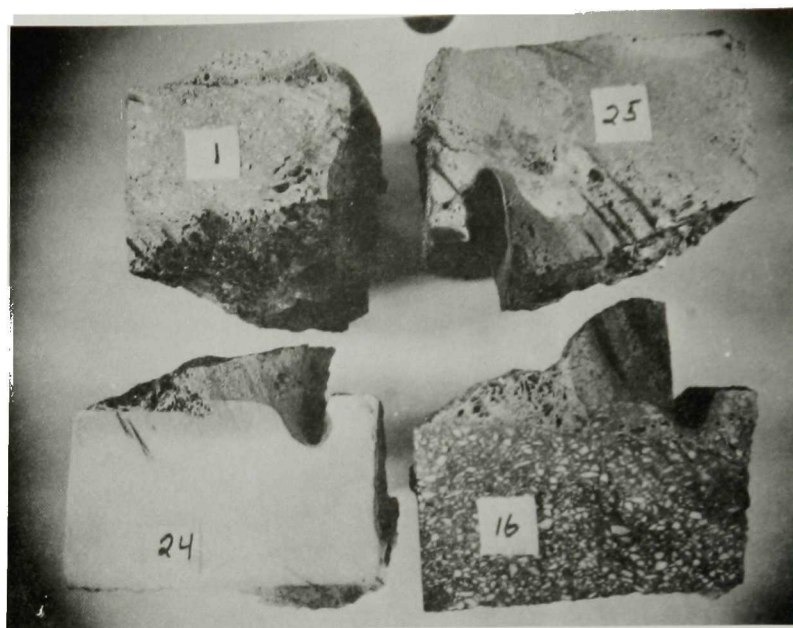
The results previously reported¹ for Run 2 are again presented in Table I. This table is included to aid in interpreting the relative resistance to slag attack exhibited by the specimens, as shown in Fig. 1. All of the half-brick specimens have been cut in half to expose their central cross sections, which were originally 65-75 mm (2 1/2-3 in.) thick by ~ 110 mm (4 1/2 in.) wide. The specimens are arranged in related groups such that the surface exposed to the slag lies toward the center of the group. Figure 1a shows the four high-alumina sinter-bonded refractories. Of these, only the alumina-chrome and the 97.6% alumina specimen exhibited small penetration and abrasion depths. Figure 1b shows the magnesia-chrome and silicon carbide type specimens. The magnesia-chrome specimens performed well, but the silicon carbide types performed poorly. The problem with the latter may be attributed to the small thermal gradient across the specimen. This type of specimen will be retested later with a greater thermal gradient.

Figure 1c shows the phosphate-bonded aluminas. With the possible exception of the specimen that contains chrome, this group was almost completely penetrated by the slag. The last group of the specimens, all fusion cast, are shown in Fig. 1d. It is evident that little corrosion

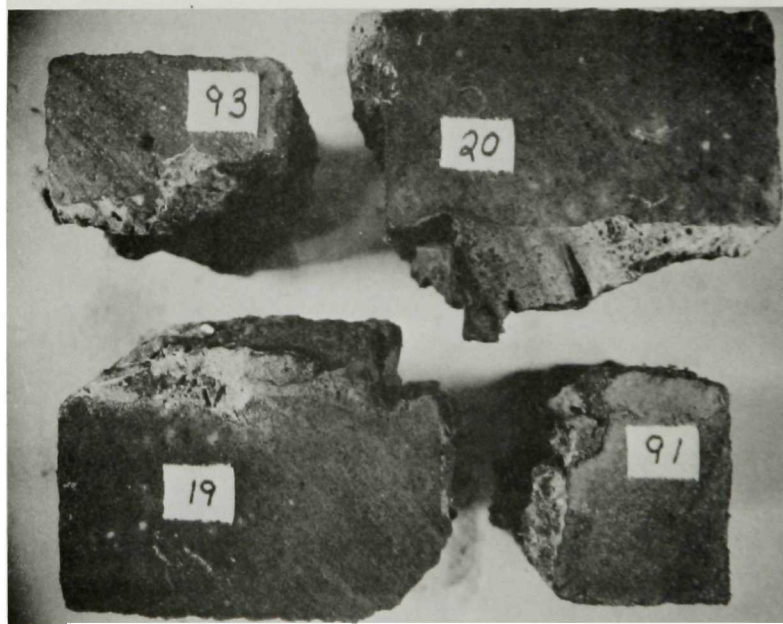
TABLE I. Refractories Exposed in Slag-abrasion-corrosion Rig Run 2^a

Identification Number	Composition	Bond	Normalized Material Lost, vol %	Maximum Depth of Penetration, mm	Maximum Depth of Abrasion, mm	Remarks
1	Al ₂ O ₃ (99%)	Sintered ↓	28.9	64	57	-
24	Al ₂ O ₃ (97.6%)		4.5	~18	17	-
25	Al ₂ O ₃ (99.5%)		9.4	76	~25	-
16	Al ₂ O ₃ (90%)-Cr ₂ O ₃ (10%)		8.2	~25	~10	-
19	MgO (53%)-Cr ₂ O ₃ (19%)		2.3	~10	~5	-
20	MgO (59%)-Cr ₂ O ₃ (19%)		1.6	~10	~5	-
91	SiC (79%)-Si ₃ N ₄ (18.5%)		~100	64	64	Reduced to metal
93	SiC (73%)-Al ₂ O ₃ /SiO ₂ (14/11)	↓	~100	64	64	Reduced to metal
17	Al ₂ O ₃ (85%)-P ₂ O ₅ (3.6%)	Chemical ↓ (CA) (RAM)	40.3	76	64	-
28	Al ₂ O ₃ (93.3%)-P ₂ O ₅ (1.2%)		20.5	64	33	-
27	Al ₂ O ₃ /Cr ₂ O ₃ (81/10)-P ₂ O ₅ (6.7%)		5.9	43	18	-
202	Al ₂ O ₃ (Winnofos Bond)		45.5	76	56	-
2	Al ₂ O ₃ (99%)-Na ₂ O (0.4%)	Fusion Cast ↓	7.2	~0.5	19	-
4	Al ₂ O ₃ (99%)-B ₂ O ₃ (0.5%)		8.3	<2.5	22	-
22	Spinel (65%)-R ₂ O ₃ (~30%)		Neg	Neg	Neg	-

^aCA = castable, RAM = ramming mix, and Neg = negligible.

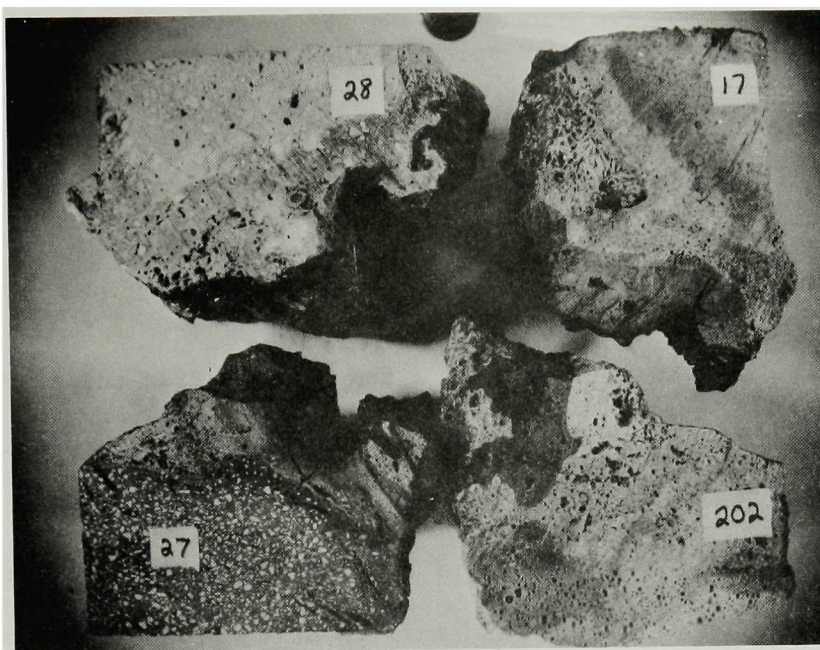


(a)

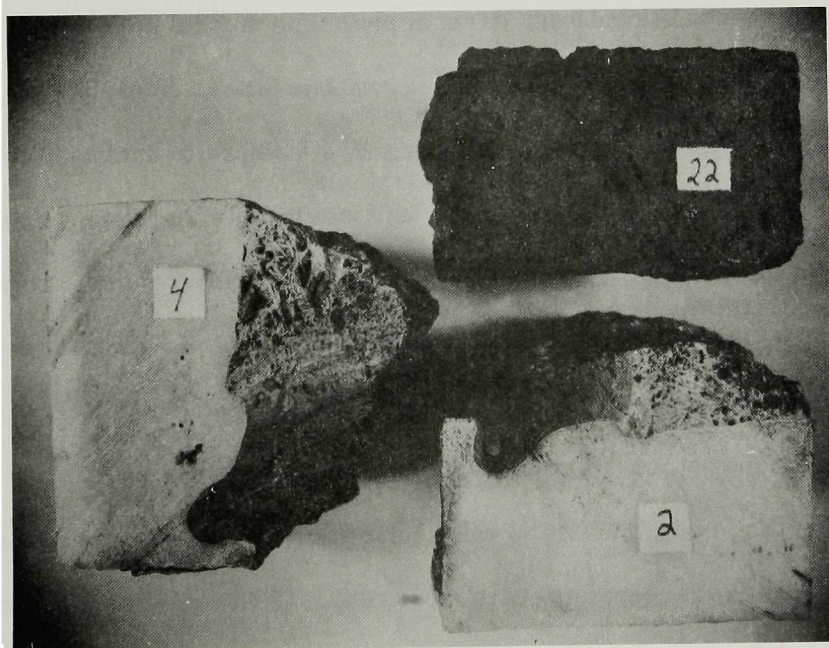


(b)

Fig. 1. Slag Attack Exhibited after Run 2 for (a) High-alumina Sinter-bonded, (b) Magnesia-Chrome and Silicon Carbide Type, (c) Phosphate-bonded Alumina, and (d) Fusion-cast Specimens. Neg. Nos. MSD-63567, 63568, 63565, and 63566.



(c)



(d)

but some cavitation-type abrasion has occurred for the two fusion-cast aluminas. The fusion-cast spinel- R_2O_3 brick, on the other hand, exhibited negligible interaction after the 500-h test.

Samples of all the specimens have been shipped to the vendors for additional analysis. At the same time, microscopic examination of the more resistant specimens is continuing.

The change in slag chemistry as a function of time during Run 2 can be obtained from the composition data in Table II. After approximately the first 150 h, the slag chemistry did not change appreciably. The early changes, principally the reduction of alumina and silica, were probably due to the precipitation of alumina and mullite at the lower edges of the slag pool, which are cooler than the center. This will be investigated by a chemical analysis of the solidified slag.

To obtain thermal-gradient data across the brick specimens during the test, holes were drilled radially from the steel shell to the cold face of three bricks. These bricks encompassed a range in thermal conductivity from low (aluminum zirconium silicate and periclase chrome) to high (silicon oxynitride). The average measured thermal gradients ranged from 200-250°C during the first 100 h of Run 3. A rough calculation indicates that these gradients are one-third to one-half of the gradient calculated for a similar radial position of a 230-mm (9 in.) wedge brick with a water-cooled cold face. The gradients will be determined when the construction of the new bottom furnace segment is completed. This segment contains a water-

TABLE II. Slag Composition (wt%) during Run 2^a

Component	Time, h								Average
	0 ^b	86	158	186	278	375	422	494	
Al ₂ O ₃	13.76	21.25	15.9	13.60	15.20	15.30	15.40	13.44	15.7
CaO	34.0	31.96	39.60	41.0	38.46	36.56	39.52	37.18	37.8
SiO ₂	39.20	28.75	22.90	24.20	25.56	26.04	23.68	25.26	24.9
SO ₃	0.106	0.025	0.035	0.037	0.022	0.022	0.025	0.025	0.03
Fe ₂ O ₃	6.97	7.01	10.17	8.86	9.73	8.54	10.06	10.39	9.2
MgO	3.62	5.82	8.84	9.54	8.85	8.68	9.26	9.28	8.6
K ₂ O + Na ₂ O	0.5-1.5	0.5-1.5	0.5-1.5	0.5-1.5	0.5-1.5	0.5-1.5	0.5-1.5	0.5-1.5	~1.0
TiO ₂	0.46	0.35	0.37	0.30	0.31	0.31	0.31	0.30	0.3
V ₂ O ₅	0.03	0.03	0.01	0.02	0.02	0.01	0.05	0.05	0.03
Cr ₂ O ₃	0.05	-	0.06	0.18	0.09	0.17	0.11	0.17	0.13
P ₂ O ₅	0.83	0.59	0.85	0.84	0.95	0.93	0.93	0.93	0.86

^aAverage base/acid ratio was 1.6.^bSlag composition was adjusted after 72 h.

cooled backing plate that provides direct coupling to the cold face of the bricks. In this new design, full and partial wedge bricks will be utilized to determine the effect of the thermal gradient on the degree of slag penetration and abrasion.

Task B -- Evaluation of Ceramic Coatings for Coal-conversion Plants
(Principal Investigator: D. Stahl)

Several of the metallic specimens with partial or total coatings were examined after exposure to high-velocity (~ 38 m/s) char particles at 980°C and a pressure of 240 kPa (35 psi). The exposure was conducted in the ERDA-owned corrosion-erosion furnace by Solar, Inc. After photographing the front and back faces of the U-bend specimens, the specimens were cut and mounted for microscopic examination. From the exposed edges, the thicknesses of the remaining coatings were obtained. These are listed in Table III.

As noted in the previous quarterly report,¹ only the metallic specimens coated with magnesium zirconate survived the exposure. This coating exhibited nonuniform coverage as shown in Fig. 2; however, no chemical attack was observed. Of the remaining specimens examined, only the Type 310 stainless steel coated with zirconia retained the coating, but only on the back face. The coating on the front face of this specimen and the remaining coatings spalled.

Task C -- Nondestructive Testing of Coal-plant Components (Principal Investigators: W. A. Ellingson, G. C. Stanton, W. J. Shack, N. P. Lapinski, and R. F. Vogt)

1. Erosion Detection and Monitoring

During the present quarter, efforts on the application of ultrasonic methods to measure erosion have been made in two areas: (a) continued

TABLE III. Wear of Coated Metal Specimens after 100-h
Exposure to High-velocity Char at 980°C

Coating Material	Substrate	Coating Thickness, mm	
		Back Face	Front Face
Al_2O_3	Type 304 SS	0.07	0.11
	Incoloy 800	0.01	0
	Type 310 SS	0	0
MgO-ZrO_2	Type 304 SS	0.30	0.11
	Incoloy 800	0.30	0.07-0.27
	Type 310 SS	0.28	0.10-0.23
ZrO_2	Type 310 SS	0.27	0.08
Cr_2O_3	Type 310 SS	0.04	0.05
$\text{Al}_2\text{O}_3\text{-Cr}_2\text{O}_3$	Type 310 SS	0.06	0.03

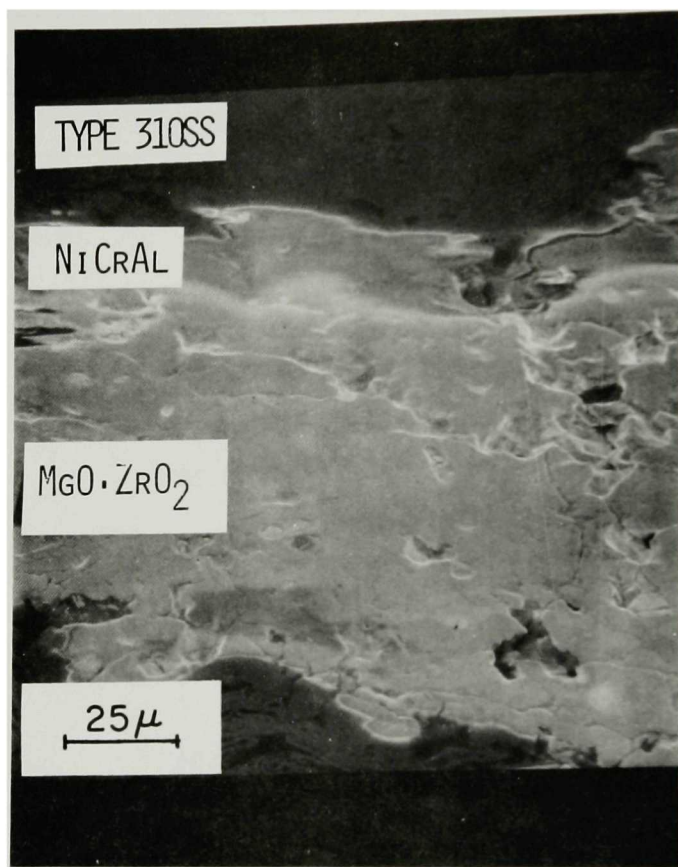


Fig. 2. Exposed Surface of Magnesium Zirconate-coated Specimen. Neg. No. MSD-63564.

mapping of the HYGAS high-pressure cyclone and (b) additional development of ultrasonic pulse-echo techniques for the in-situ erosion-measurement system for the Bi-Gas coal-conversion (gasification) plant.

a. Laboratory Ultrasonic Studies.

A third mapping of erosion on the HYGAS high-pressure raw-gas cyclone separator was conducted in the laboratory using the pulse-echo ultrasonic technique described previously.² Approximately 1000 h of operation were completed between the second (February 1976) and third mappings. Ultrasonic wall-thickness measurements were made over both the Stellite-lined and unlined areas of the inlet region and encompassed a 133-point matrix as shown in Figs. 3 and 4. Ultrasonic wall-thickness measurements were also made at 16 points on the solids outlet neck (7-76 Data Layout, Fig. 3).

The most severe wall-thickness reduction observed in the cyclone inlet region occurred along circumferential band b (which coincides with the inlet centerline) and azimuthal position 5 (Fig. 4a). This reduction was ~17 mils (0.43 mm) or ~2% of the wall thickness. The wall-thickness data at each azimuthal position along circumferential band b for both the second and third mappings are plotted in Fig. 5. Of interest from the current data, however, is the wall-thickness reduction found in the solids outlet region. Twelve points, using bands B, Γ , and Δ of the 7-76 layout (Fig. 3) at four azimuthal positions (Fig. 4b), were ultrasonically measured as in the previous mapping, and the results are plotted in Fig. 6. The greatest amount of erosion, 80 mils (2.03 mm), 17.7% of

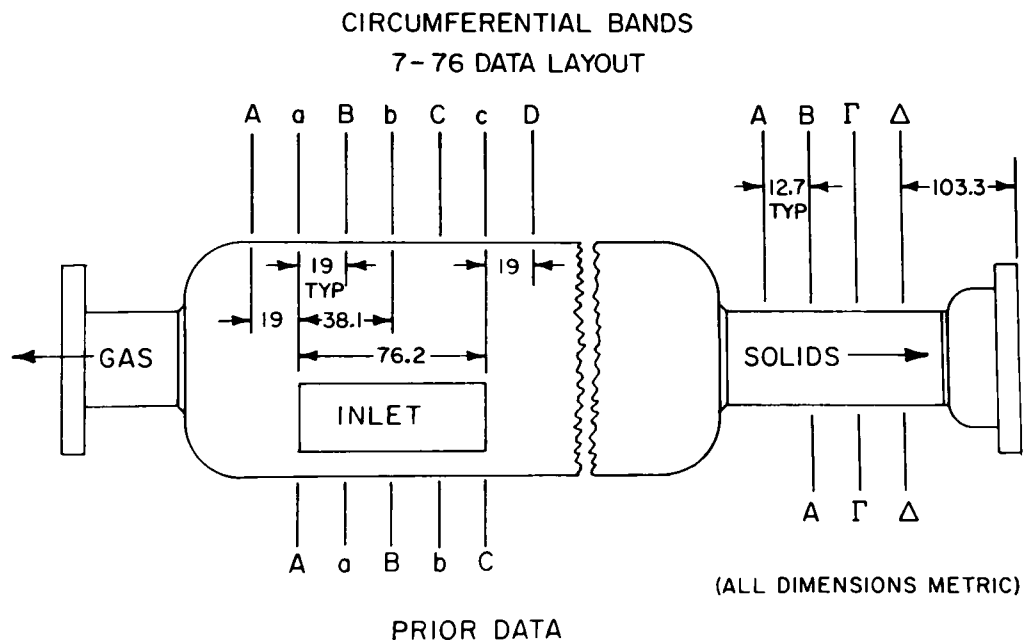


Fig. 3. Schematic Diagram of HYGAS High-pressure Cyclone Showing Longitudinal Location of Erosion Mapping Positions. Neg. No. MSD-63457

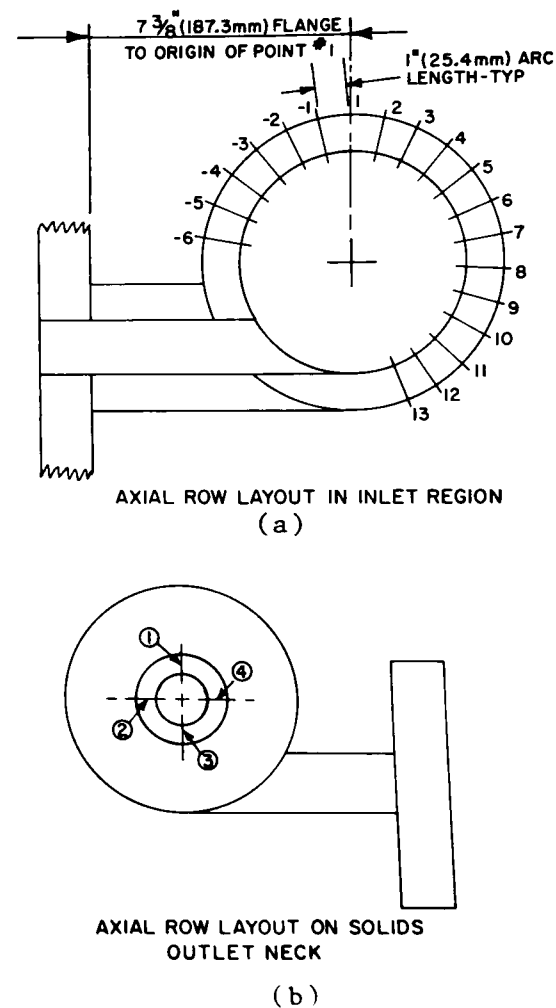


Fig. 4. Schematic Diagram of HYGAS High-pressure Cyclone Showing Azimuthal Location of Erosion Mapping Positions. Neg. No. MSD-63456.

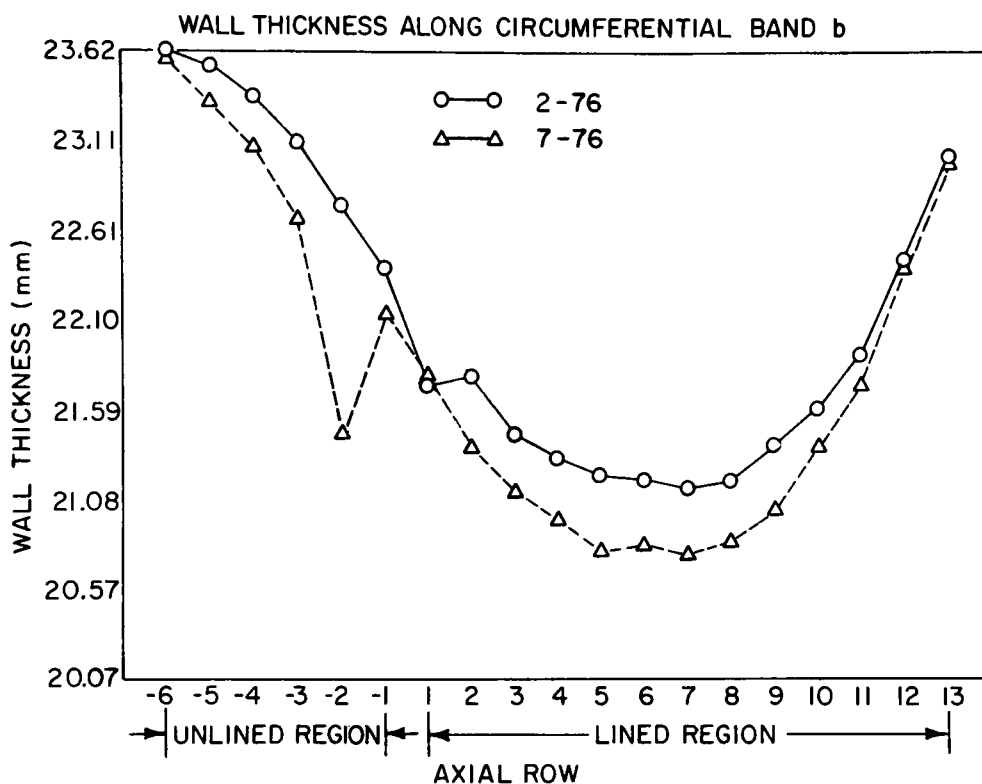


Fig. 5. Apparent Wall Thickness of Inlet Region of High-pressure Cyclone at Longitudinal Position b. Neg. No. MSD-63454.

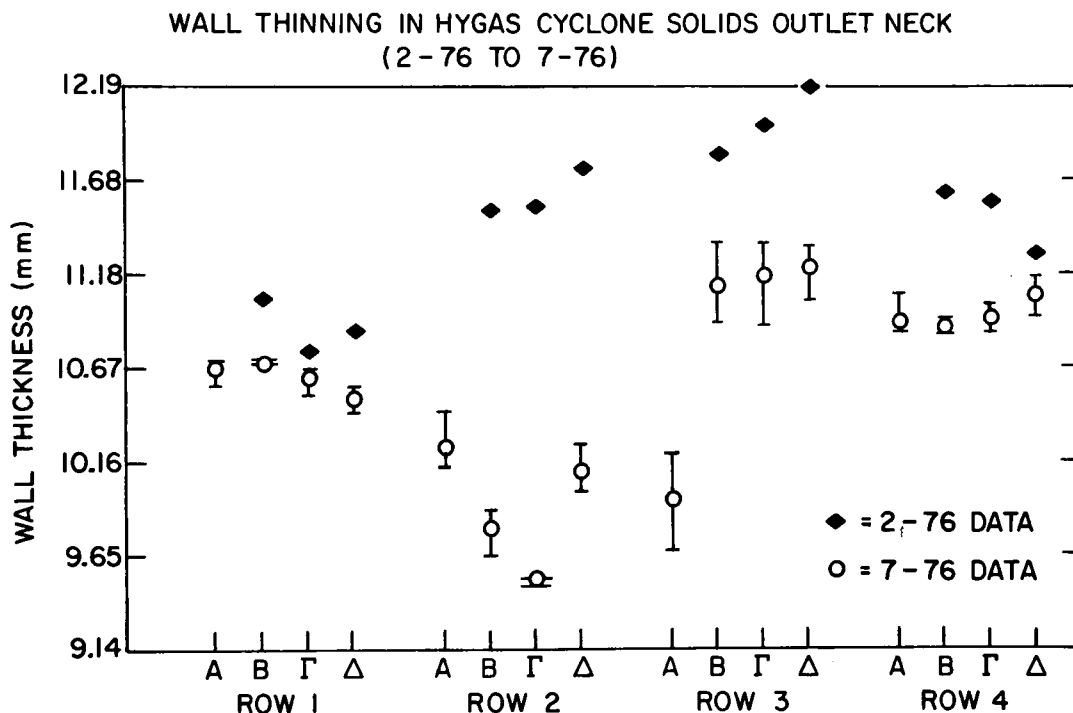


Fig. 6. Apparent Wall Thickness of Solids Outlet Region of High-pressure Cyclone as a Function of Longitudinal Position. Neg. No. MSD-63455.

of the wall thickness, was detected at azimuthal position 2 of circumferential band Γ . The average wall-thickness reduction of the 12 points measured was 24.4 mils (0.62 mm).

Because of the desire to more completely map the erosion pattern in the cyclone, additional locations at both the inlet and solids outlet regions were measured for future comparison. These are shown in Fig. 3 (7-76 Data Layout).

b. In-situ Erosion Detection Using Ultrasonic Techniques.

This project was continued during the present quarter primarily by finalizing details for the field installation at the Bi-Gas pilot plant. The details included (1) determination of the exact monitoring locations, (2) fabrication of an explosion-proof pressure chamber designed to contain the ultrasonic pulser-receiver and equipment for continuous recording of wall thickness, (3) fabrication of the 31 high-temperature waveguides, (4) development and construction of the specially designed electronic scanning system, and (5) personnel arrangements to avoid conflict of interests among labor unions.

The locations of waveguide installation are shown schematically in Fig. 7. The layout of the in-situ measurement system for locations 1 and 2 is shown in Fig. 8. More monitoring positions are located where angles of impact are expected to be from 35-50° since the majority of oblique-impact-angle erosion data indicate that the most severe erosion for multiphase flow occurs in this range. The monitoring positions for location 2 are identical to those for location 1 with respect to the flow direction.

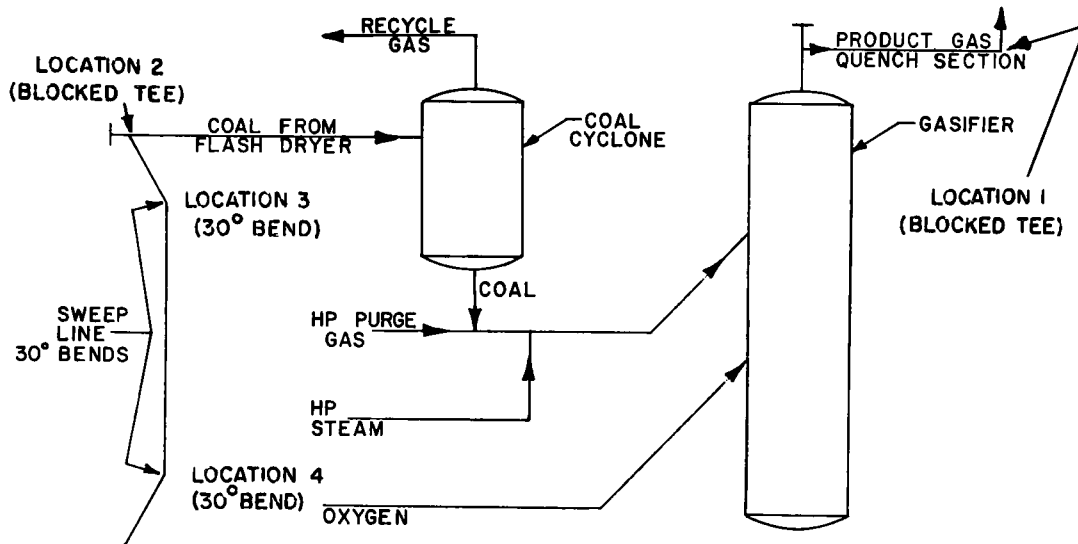


Fig. 7. Schematic Diagram of Bi-Gas Coal-conversion System Showing Placement of In-situ Erosion-measurement Locations. Neg. No. MSD-63393.

8-in. SCHEDULE 140 TYPE 304 SS
 OD=8.625, ID=7.001, WALL THICKNESS= 0.812
 T=800°F, P=1150psi, f= 25 ft s

BI-GAS PRODUCT GAS LINE
 BLOCKED TEE NUMBERS 182
 11 WAVEGUIDES

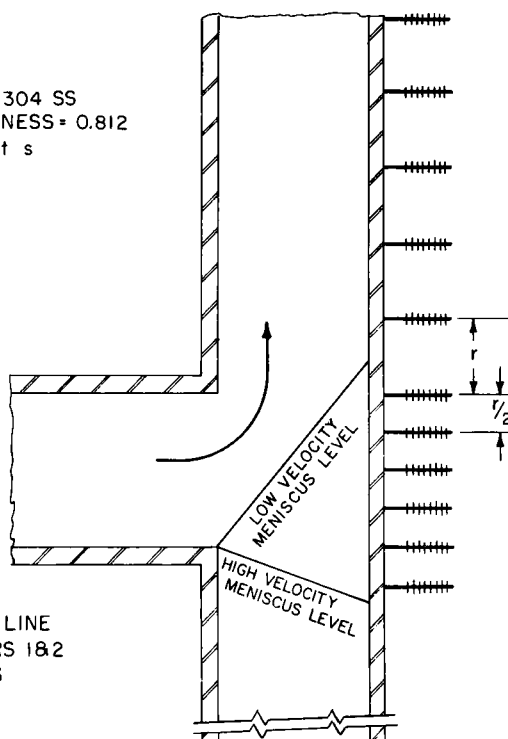


Fig. 8. Schematic Representation of Erosion-measurement Positions for Product-gas Transfer Line and Coal-feed Transfer Line Blocked Tees. Dimensions are in inches. Neg. No. MSD-62997.

The monitoring positions (5 each) at locations 3 and 4 are shown in Fig. 9. The reference position at all locations is the intersection of the centerline of the incoming flow line with the wall of the adjacent upstream piping. Each waveguide is fitted with copper fins for convective air cooling as described in a previous quarterly report.² The air-cooled waveguides have been fabricated, and a contract has been let with a commercial stud-welding firm to field weld the waveguides to the pipes and blocked tees using capacitive-discharge techniques described previously.³ The instrumentation system shown in Fig. 10 includes (1) a commercially available ultrasonic pulser-receiver fitted with a time-analog-gate digital thickness readout, (2) a dual-channel strip-chart recorder with an event marker for indication of the reference-position transducer, (3) thermocouples on both the pipe wall and transducer site, and (4) a specially designed electronic scanning system with a continuously variable sampling-time control and digital computer interface. All system components have been received and are being tested.

The field installation will begin in October and be completed by the end of November 1976.

c. Erosion and Hot-spot Detection by Infrared Methods.

During this quarter, development of the use of digital image processing of black and white photographs taken from infrared imaging systems has continued. Initial work was discussed in the previous quarterly report.¹ Details of the work conducted during the present quarter will be described in depth in the next report.

10 inch A 106 B
SCHEDULE # 120

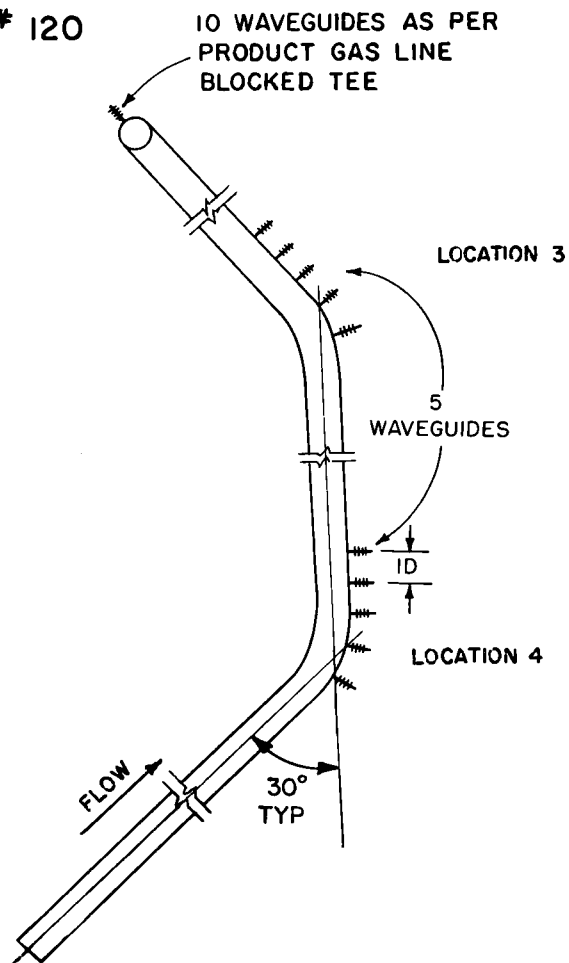


Fig. 9. Schematic Representation of Erosion-measurement Positions for Bi-Gas Coal-feed Transfer Line. Neg. No. MSD-62999.

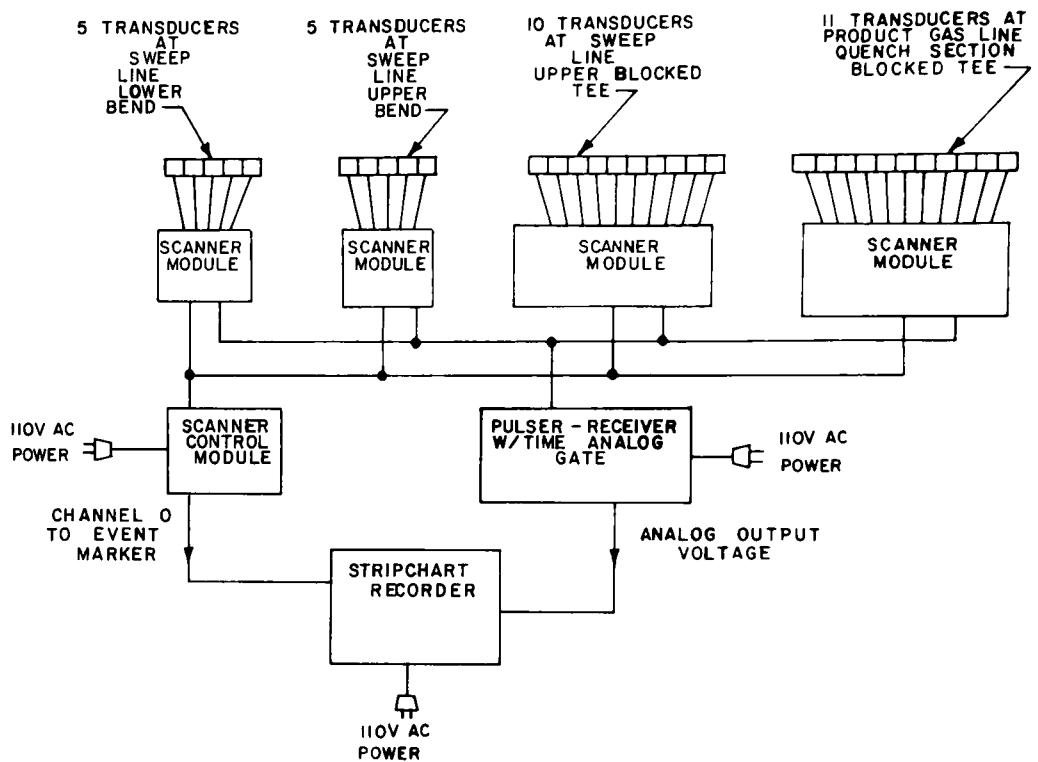


Fig. 10. Block Diagram of In-situ Ultrasonic Erosion-measurement Instrumentation for the Bi-Gas Coal-gasification Pilot Plant. Neg. No. MSD-63392.

2. Refractory-installation Studies

a. Acoustic-emission Studies for Control of Refractory Curing.

The use of acoustic emission for detection of cracking of refractory specimens, which can be applied to refractory-installation procedures, has been under development for several months. Previous work⁴ has shown that relationships between acoustic-emission parameters (such as acoustic-emission counts per unit fracture area and total counts) and crack growth can be determined. The relationship between refractory integrity and longevity in coal-conversion system environments and refractory curing schedule, however, is yet to be established. Thus, the extent of cracking in refractories that results from various heat-up schedules is being investigated using acoustic-emission monitoring.

Initial studies on crack detection in refractories have been conducted using simply supported beam specimens and resonant* transducers. Initially, three-point load tests were conducted, but the small area in contact with the specimen did not permit sufficient coupling to transmit the acoustic energy. In addition, a quiet loading fixture was necessary to ensure that the acoustic emission of interest was in fact generated by the fracturing of the refractory specimens.

During the past months, these problems have been somewhat overcome. The noise in the loading fixture was eliminated through design of a pneumatic load system. A data-acquisition system (Fig. 11), which permits recording of the rapidly occurring events, was assembled. The main component of the system is the magnetic tape recorder, which has a

*Center frequency = 175 kHz with a 100-kHz bandwidth.

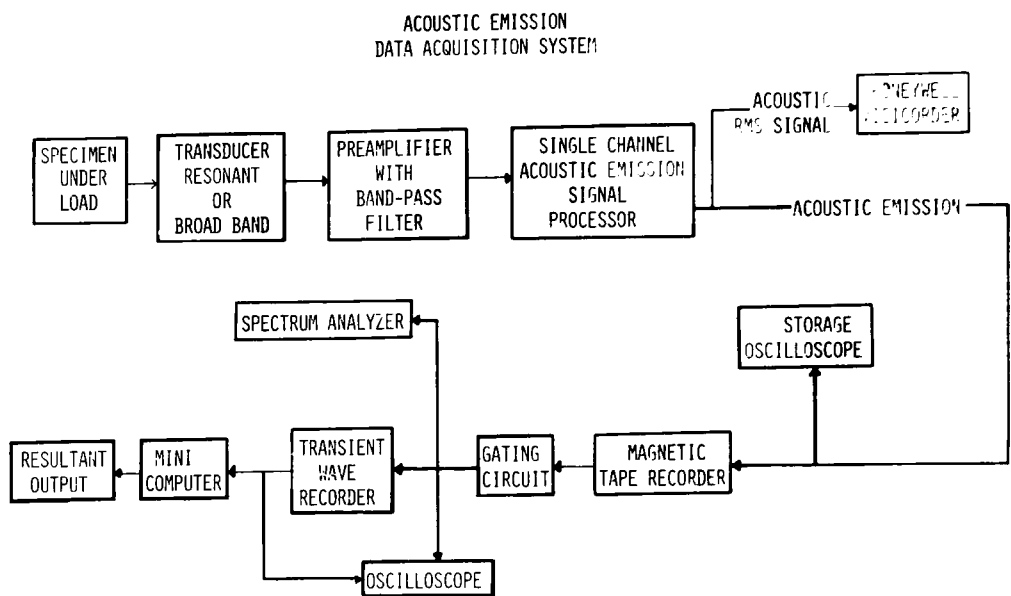


Fig. 11. Block Diagram of Instrumentation System Used for Acoustic-emission Studies of Refractory Specimens. Neg. No. MSD-63429.

unique gating circuit that facilitates examination of only the signal portion of interest. In addition, the tape recorder has a special "stop-action" gating, which will permit display of any 17.5-ms segment of the recording. The gated segment then can be used for thorough ringdown or spectral analysis of a single event. The output of the gated signal segment can be analyzed for frequency content by use of a spectrum analyzer or can be digitized for subsequent analysis by an analog-to-digital converter. The digitized signals can be employed in signal-averaging routines or can be subsequently used for comparison of individual signals from different specimens.

Figure 12 shows a schematic of the loading fixture and specimen used for initial laboratory experiments. The samples were prepared by mixing the refractory to a "ball-in-hand" consistency. The refractory was poured in an aluminum mold (Fig. 13), which was subsequently placed on a mechanical vibrator for ~5 min to remove the trapped air. The samples were dried in air for 72-96 h prior to mechanical testing. The resultant specimens had dimensions of 6.34 x 31.75 x 127 mm.

Typical acoustic signals emitted from refractories under load are shown in Fig. 14. We have characterized these signals into two types. Type I is normally observed prior to complete fracture and is characterized by a short ringdown time and a long period between separate pairs of acoustic bursts. Type II signatures are observed when the crack is propagating completely through the specimen.

Analysis of the data has shown that a clear relationship exists between refractory density and the acoustic-emission parameters counts per event (C/E) and root-mean-square (rms) signal level. The

ACOUSTIC EMISSION

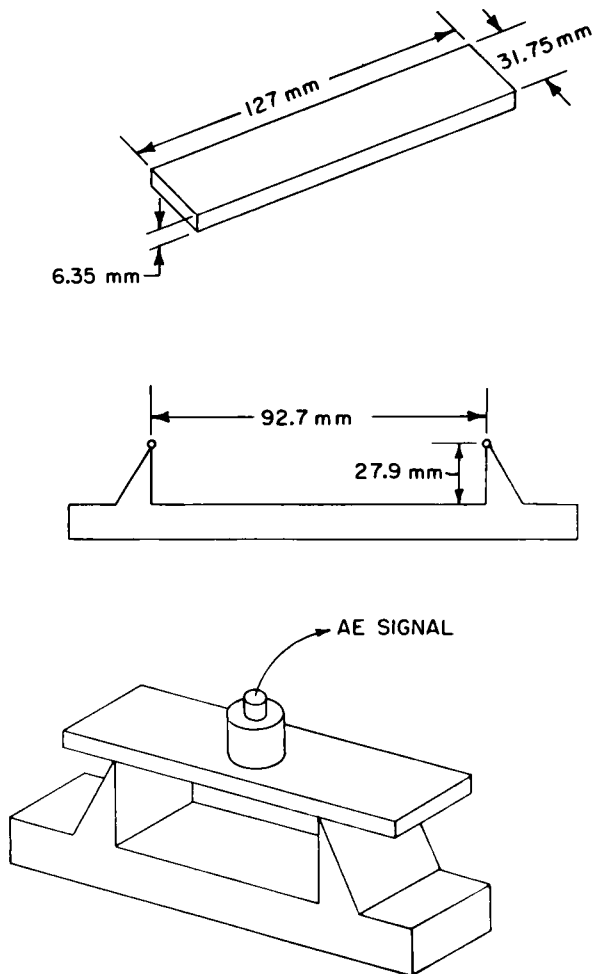


Fig. 12. Schematic Diagram of Loading System Used to Characterize Acoustic-emission Signals from Refractories.
Neg. No. MSD-63427.

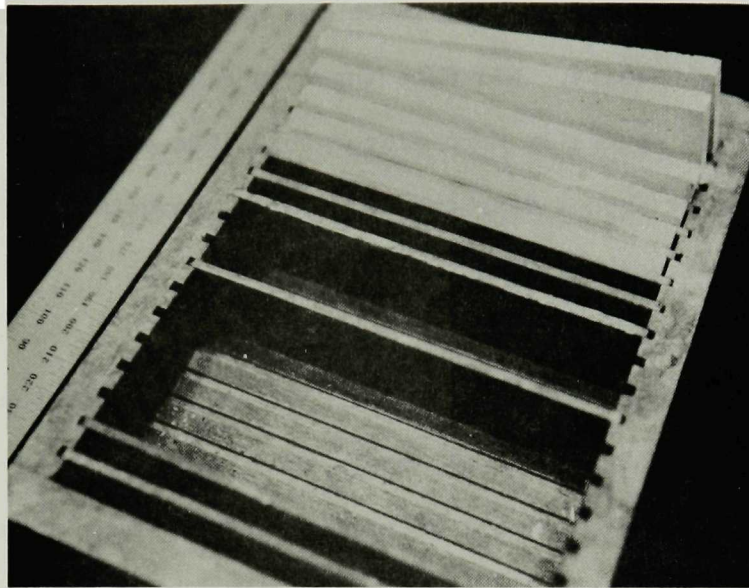
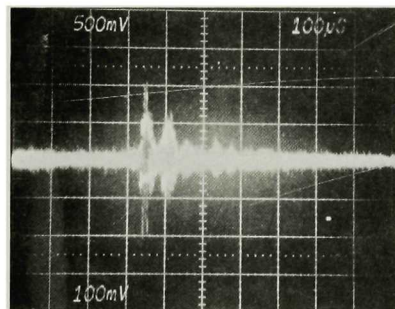
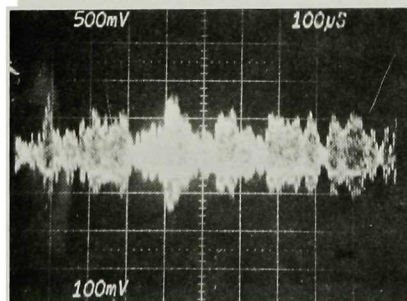


Fig. 13. Photograph of Mold Used to Prepare Refractory Specimens. Neg. No. MSD-63425.



TYPE I EVENT

SHORT RINGDOWN TIME,
LONG SEPARATION TIME



TYPE II EVENT

LONG RINGDOWN TIME,
SHORT SEPARATION TIME

Fig. 14. Acoustic-emission Signals Emitted from Refractory Specimens under Load. Neg. No. MSD-63424.

relationship is shown in Fig. 15, where rms signal and C/E are plotted versus refractory density. All data shown in Fig. 15 are from Type I bursts, which were generally more discernible than a Type II event. It is anticipated that Type I data can be used to characterize cracking patterns in dual-layer refractory systems.

b. Future Plans.

Additional refractories with different densities will be tested. Samples cut from the full-scale mock-up section and cured at different heat-up schedules will be studied to determine acoustic-emission characteristics.

c. Radiography Studies Related to Installation of Refractory Liners.

Evaluation of the use of penetrating radiation to detect defects in various refractory-lined structures by the use of gamma radiography has continued this quarter. A second refractory/steel laminate mock-up of the Battelle-Union Carbide gasifier was cast. Radiographs were generated after the refractory was dried in air for 7 h. At present, the casting has not been thermally cured because of some minor instrumentation difficulties. After the difficulties are resolved, the refractory will be cured and gamma radiographed. The two sets of radiographs will be compared to determine changes in the refractory.

(1) Field Radiography. *Bi-Gas Coal Gasifier.* A field trip was made May 4-7 to the Bi-Gas coal-gasification pilot plant in Homer City, Pennsylvania to gamma radiograph portions of the refractory-lined gasifier vessel. Figure 16 is a simplified schematic of stage 2 of the gasifier that shows the locations at which gamma radiographs were generated. Figure 17 is a schematic of the wall cross section of location 2. The 90.4-mm-thick

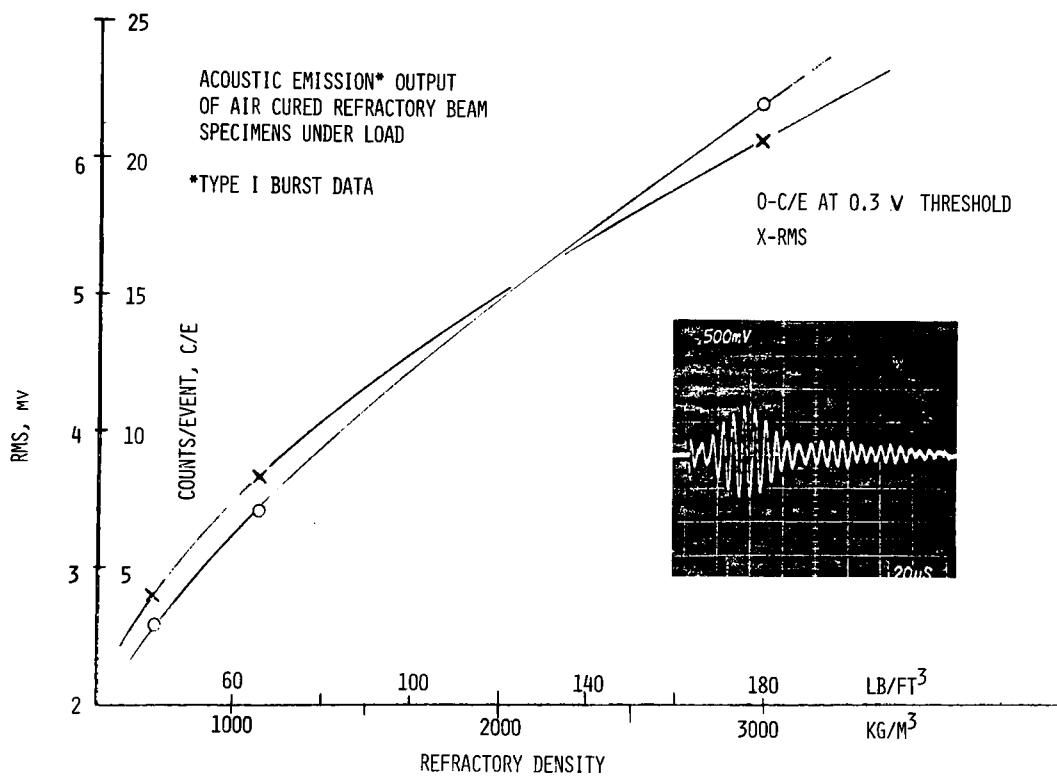


Fig. 15. Relationship between Acoustic-emission rms Levels and Type I Event Counts as a Function of Refractory Density. Neg. No. MSD-63428.

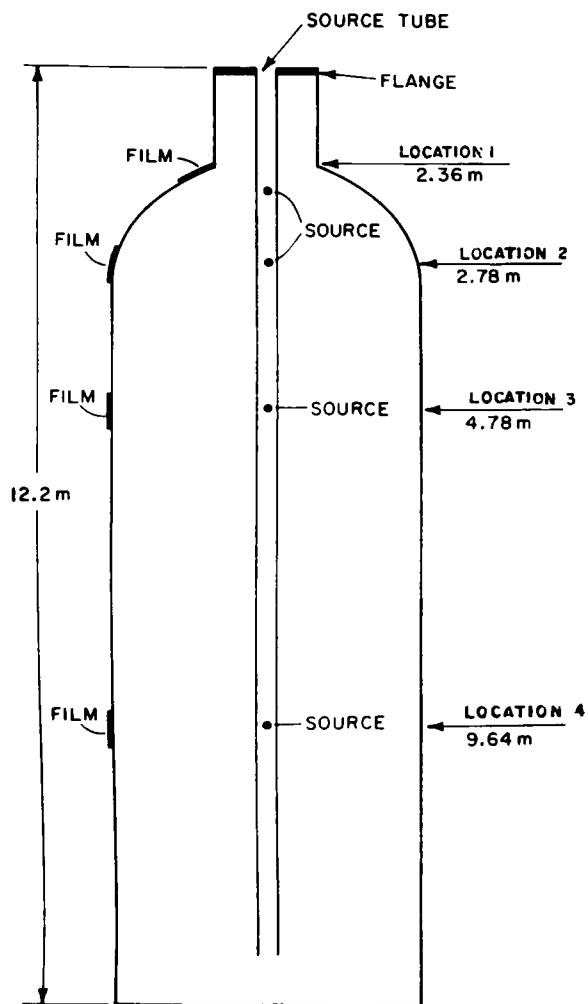


Fig. 16. Simplified Schematic of Gasifier Vessel Showing Locations at Which Panoramic Gamma Radiographs Were Generated. Neg. No. MSD-63417.

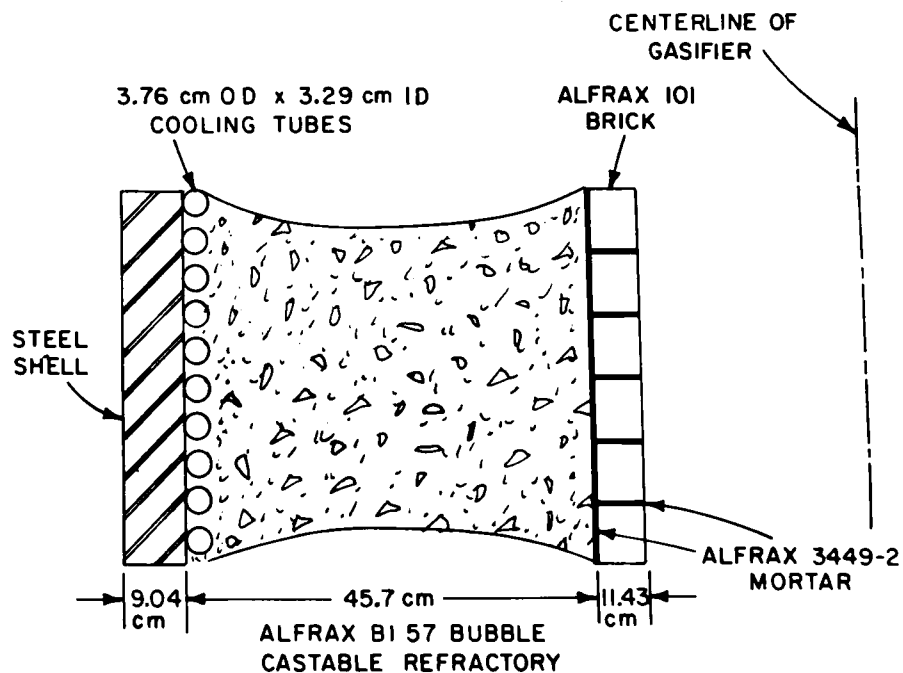


Fig. 17. Cross Section of Location 2 Obtained 2.78 m from the Top Flange of the Gasifier. Neg. No. MSD-63423.

steel shell (SA-3870) is lined with circumferential 37.6-mm outside diameter (OD) x 32.9-mm inside diameter (ID) steel (SA 213 T22) cooling tubes, which are insulated with 457 mm of ALFRAX BI57 bubble-castable refractory. The hot face (ID of the vessel) is insulated with ALFRAX 101 brick, 114.3 mm thick and set in place with ALFRAX 3449-2 mortar. Figure 18 is a schematic of the wall cross section of location 3. The 90.4-mm steel shell (SA-3870) is lined with vertical 37.6-mm OD x 32.9-mm ID steel (SA 213 T22) cooling tubes insulated with 300 mm of ALFRAX BI57 bubble-castable refractory.

The ID of the vessel is insulated with ALFRAX 101 brick 114.3 mm thick, which is set in place with ALFRAX 3449-2 mortar. Figure 19 is a schematic of the wall cross section of location 4. This cross section is identical to the one for location 3 with the exception that the thickness of the ALFRAX BI57 refractory is only 57.1 mm.

Radiographic Procedure. Using a 40-Ci ^{60}Co source, panoramic gamma radiographs were generated at four elevations of the gasifier vessel as shown in Fig. 16. Film placement for locations 2-4 is shown in Fig. 20. A 31.7-mm-diam hollow tube was secured at the top flange in the center of the gasifier to accommodate the ^{60}Co source. The use of the hollow tube made it possible for the source to be equidistant from each of the films during the time that an exposure was generated. The source-to-film distance was 711 mm for all locations. DuPont NDT-75 and Eastman Kodak Type AA film was employed with lead foil screens 0.254 mm thick at the source and back side of the cassette and 0.137 mm thick between the film. Disk-type penetrameters¹ fabricated from a high-density refractory were used for all of the exposures. Exposure times varied in each section radiographed.

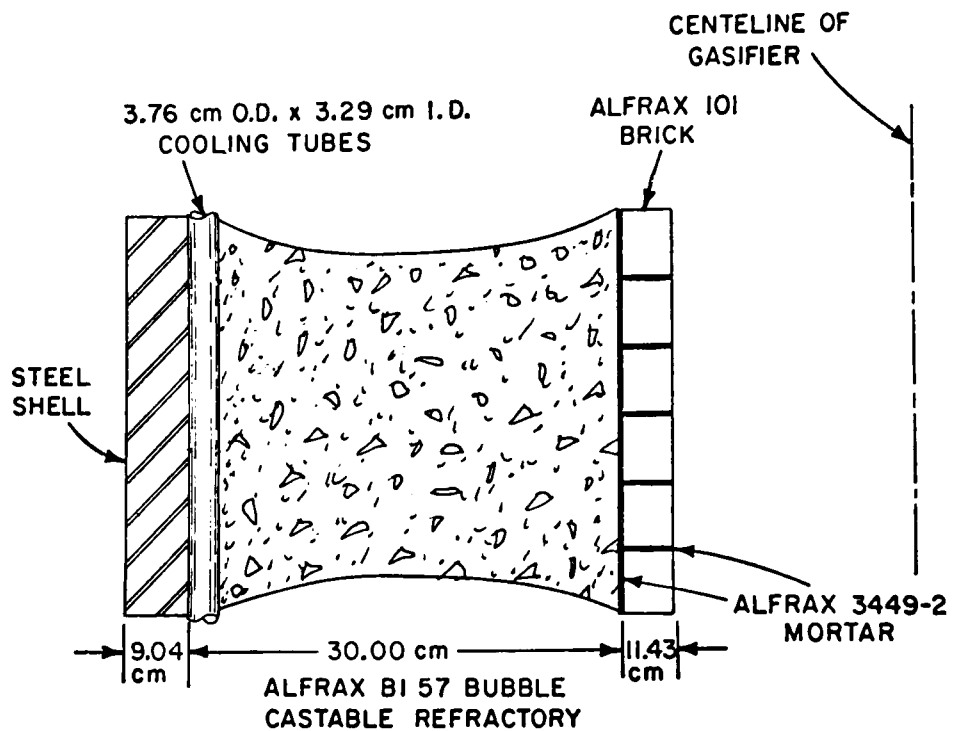


Fig. 18. Cross Section of Location 3 Obtained 4.78 m from the Top Flange of the Gasifier. Neg. No. MSD-63433.

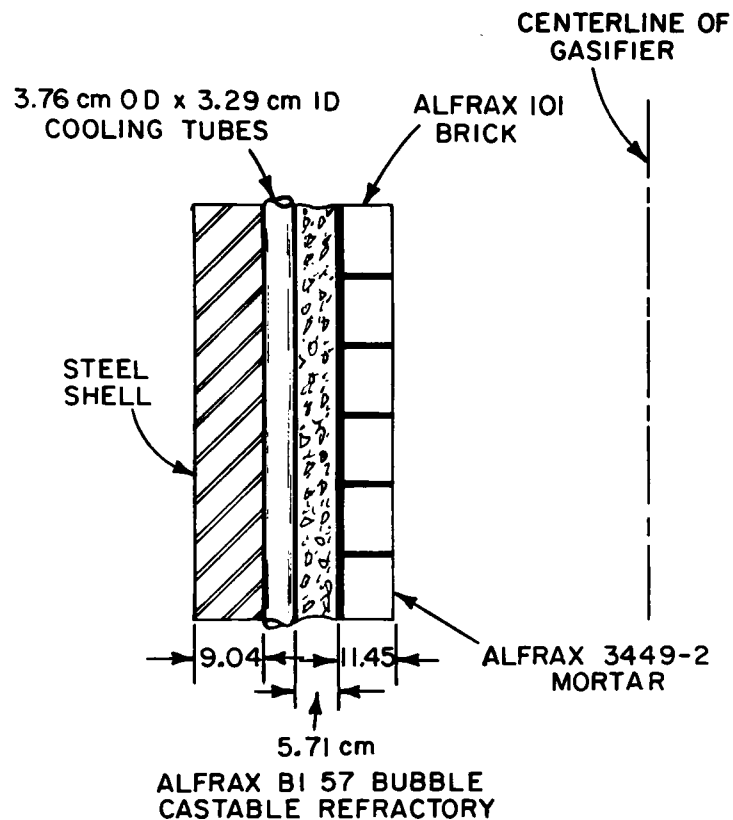


Fig. 19. Cross Section of Location 4 Obtained 9.64 m from the Top Flange of the Gasifier. Neg. No. MSD-63422.

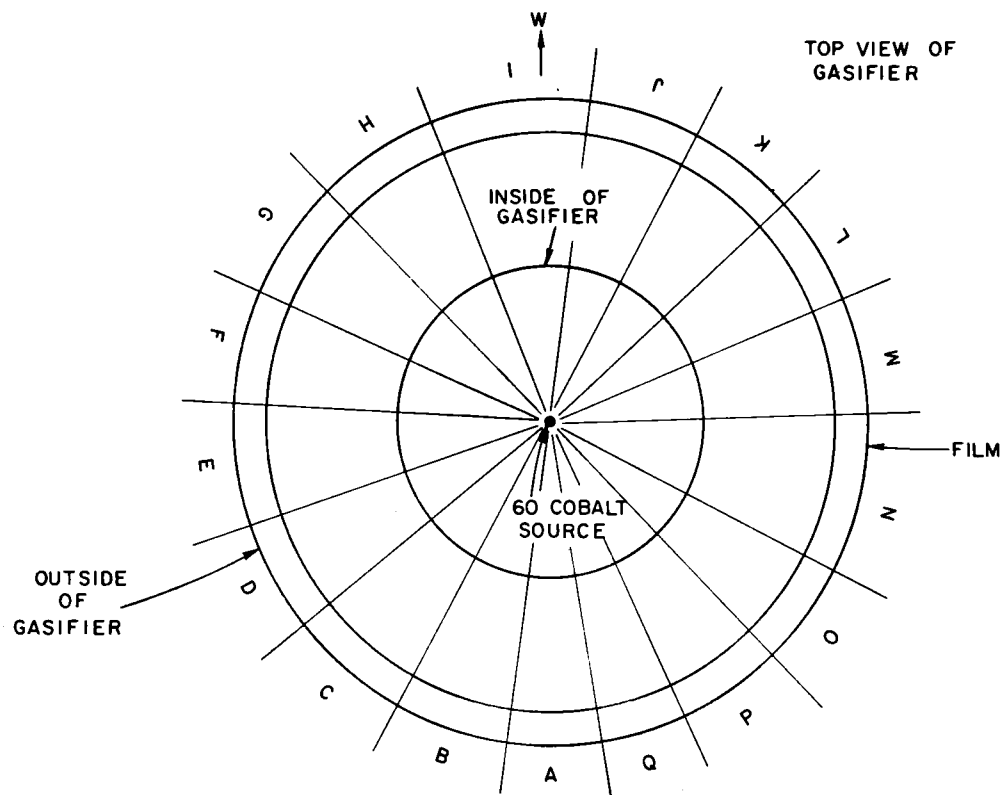


Fig. 20. Film Placement for Locations 2-4. Neg. No. MSD-63421.

The exposure time for location 1 was 20 min. Gamma-ray levels behind the film were quite intense, and no reading could be taken. The exposure for location 2 totaled 11 h, with a radiation level behind the film of 40 mR/h. Exposure time for location 3 was 5.5 h, with radiation levels behind the cassettes of 80 mR/h. All of the radiation measurements were obtained with a Victoreen Model 592 beta-gamma survey meter. This instrument is capable of reading up to 1 R/h.

Results. At location 1, the exposures were taken 2.36 m from the top flange of the vessel. Only 20% of the circumference was covered by the film at this location because mounting flanges obstructed the attachment of the film cassettes completely around the vessel. Radiographs of this area showed no abnormalities. The second set of radiographs (location 2) covered 100% of the circumference, consisted of 17 cassettes, and was taken with the source located 2.78 m from the top flange of the vessel. Mortar lines were discernible in 16 of the radiographs generated at this elevation. Figure 21 shows typical mortar lines. Figure 22 indicates details observed in this radiograph. The third set of radiographs were taken with the source located 4.78 m from the top flange of the vessel, covered 100% of the circumference, and utilized 17 films. Mortar lines were observed on 9 of the 17 radiographs as shown, for example, in Fig. 23. Figure 24 is a schematic of this radiograph. Water cooling tubes were observed with excellent clarity. Figure 25 is a typical example of a radiograph generated with the source 9.64 m from the top flange (location 4). The distance between the centerlines of the cooling tubes is shown in Figure 26. Full coverage at this elevation was not possible because of an unmovable box attached to the vessel at location K-L (Fig. 20). Only

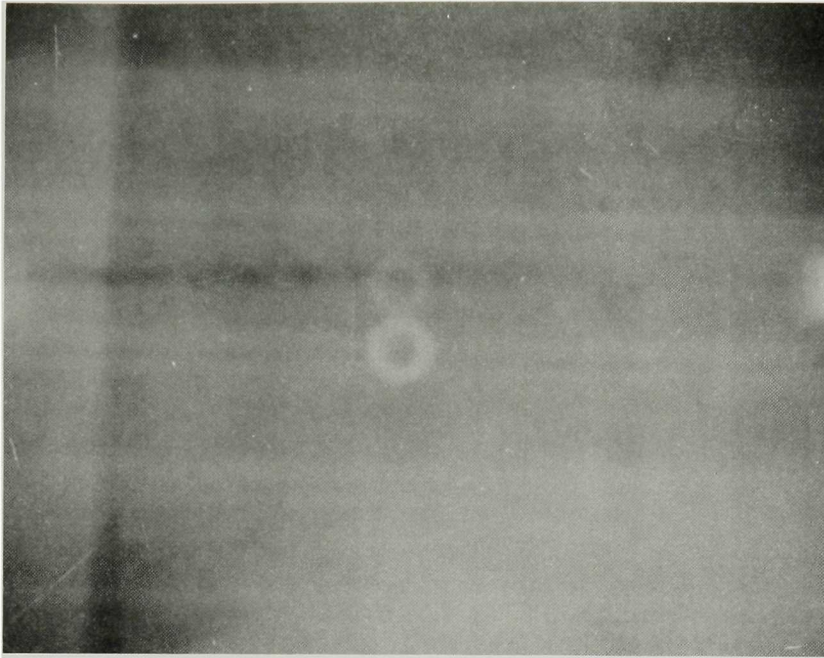


Fig. 21. Radiograph of Location 2 Showing Mortar Lines.
The round disks are penetrameters. Neg. No. MSD-62977.

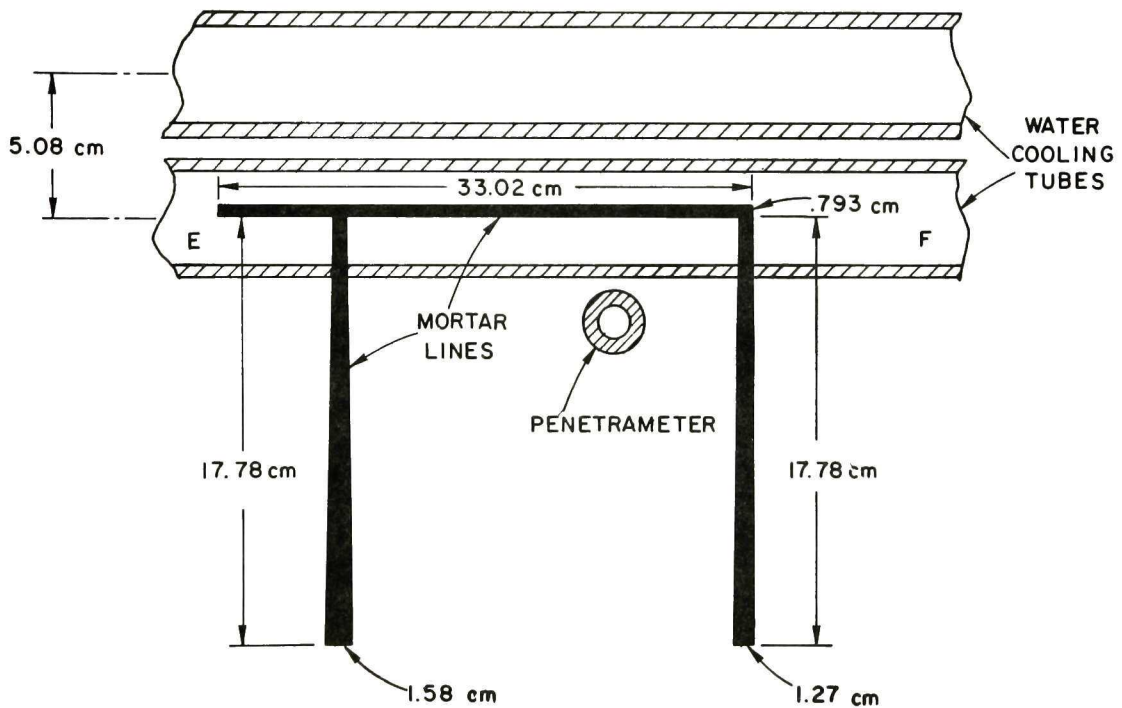


Fig. 22. Schematic of Radiograph at Location 2 Showing Details Observed.
Neg. No. MSD-63418.

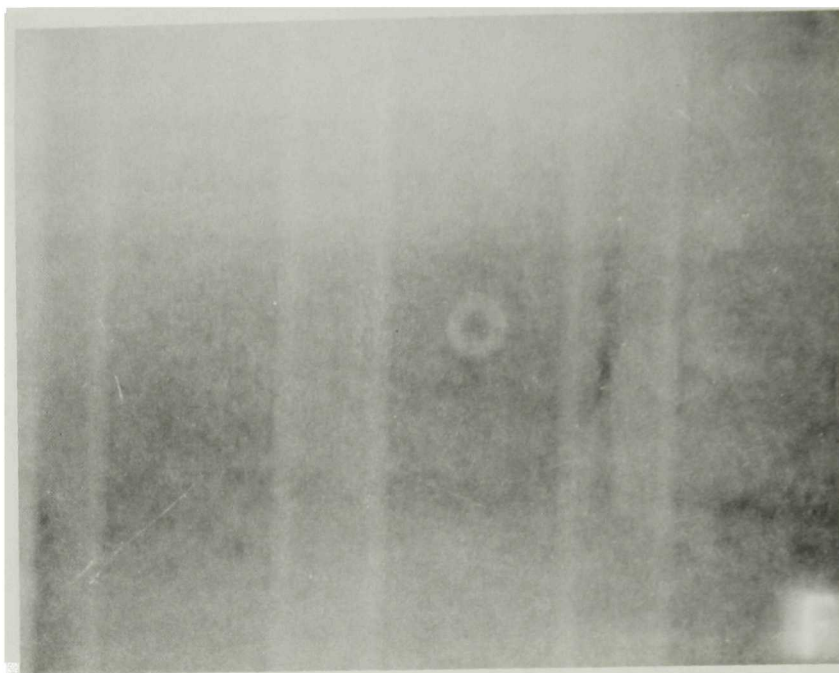


Fig. 23. Radiograph of Location 3 Showing Mortar Lines, Cooling Tubes, and Penetrameter. Neg. No. MSD-62973.

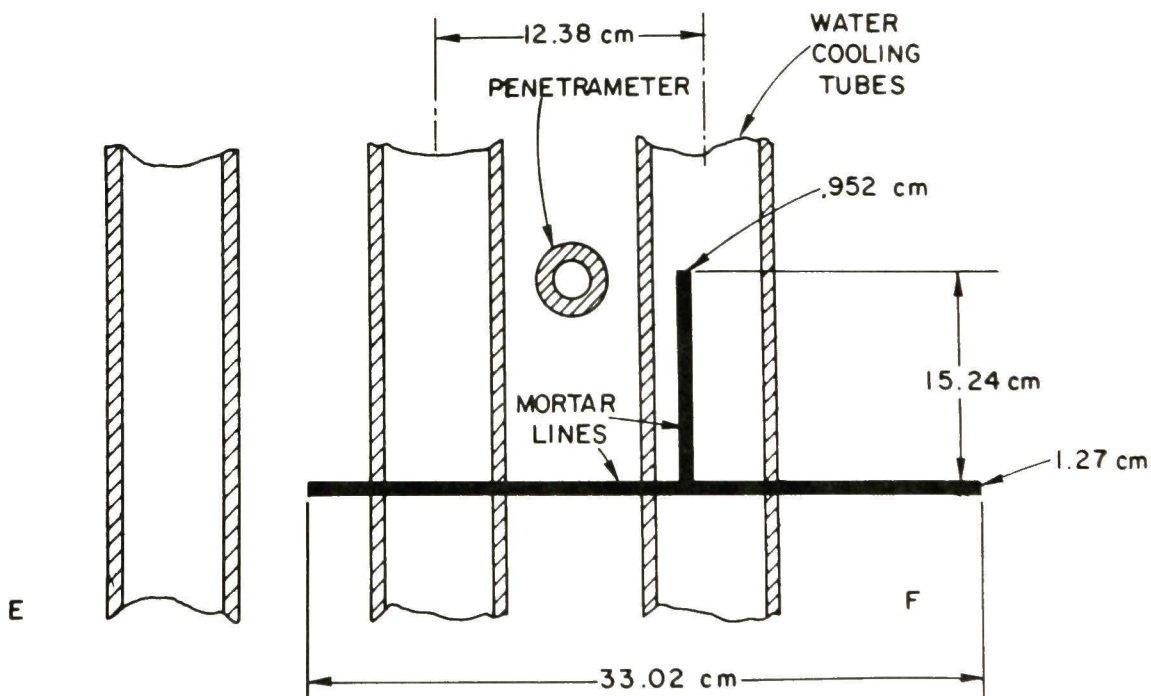


Fig. 24. Schematic of Location 3 Radiograph Showing Details Observed. Neg. No. MSD-63419.

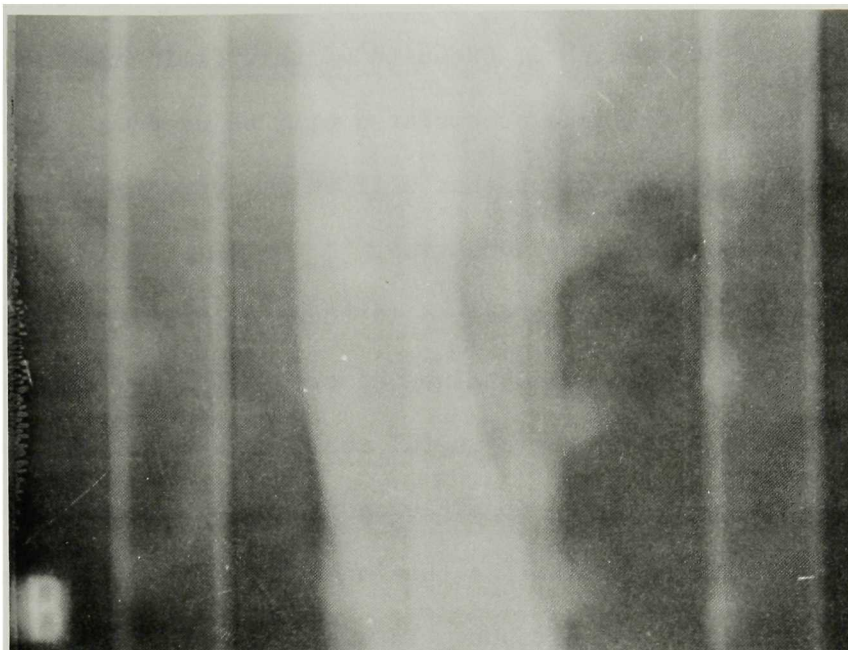


Fig. 25. Radiograph of Location 4 Showing Cooling Tubes and Penetrometer. Neg. No. MSD-62972.

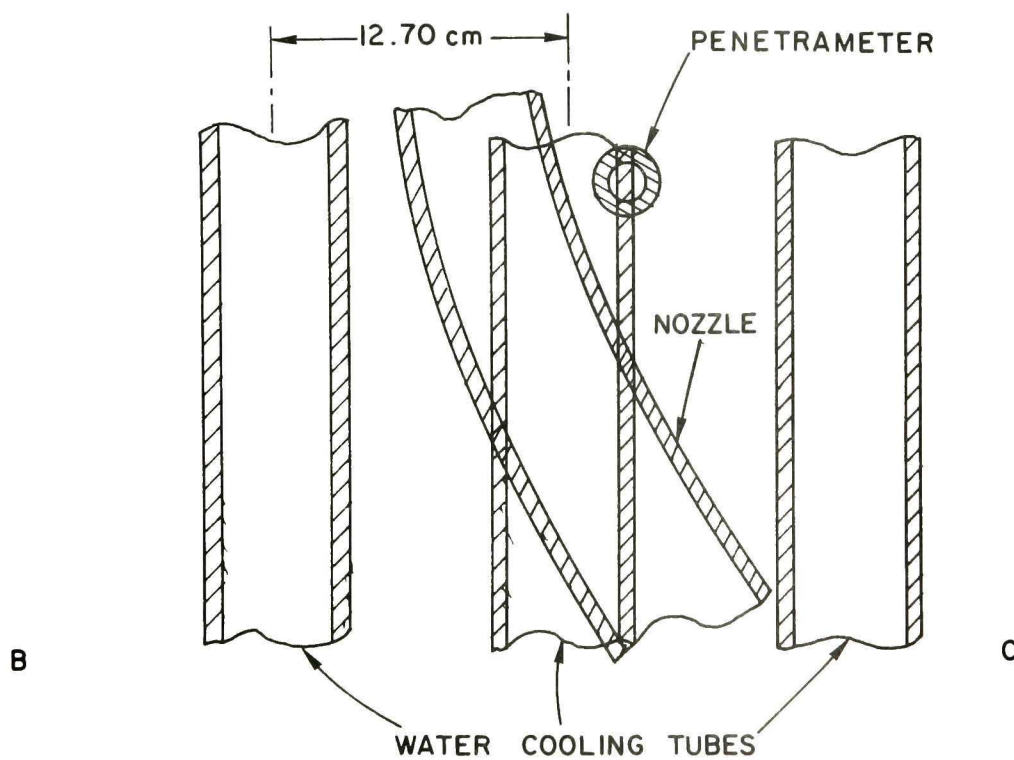


Fig. 26. Schematic of Location 4 Radiograph Showing Details Observed. Neg. No. 63420.

~95% coverage was accomplished. Results of this field examination are listed in Table IV. The data accumulated will be used as a base line for future radiographic inspections that will be performed after the Bi-Gas facility has been on line for some time.

One interesting feature observed in these examinations is the difference in radiation readings obtained at the various locations radiographed. This may prove to be a useful tool in determining thicknesses of and gross discontinuities and possible density changes in the refractory. One other item of interest is that the images of cooling tubes were clearly visible on the radiographs. Future radiographic field tests may show whether corrosive action occurs on the ID wall.

(2) Future Plans. After the refractory-steel laminate mock-up of the Battelle-Union Carbide gasifier is cured, gamma radiographs will be generated and compared with the radiographs taken before curing.

Mock-ups of areas gamma radiographed at Bi-Gas will be constructed such that emphasis can be placed on detecting corrosive action of water cooling tubes.

3. Valve Studies

a. Acoustic Leak Detection.

The effort to develop a quantitative method for acoustic leak detection has continued this quarter. Quantitative correlations have been developed for orifice plates between acoustic-emission output and mean flow parameters such as volume flow rate. A preliminary study of the acoustic coupling between valves in series was also conducted.

The experiments with orifice plates have shown that for a fixed orifice geometry a good correlation exists between the mean flow

TABLE IV. Results of Bi-Gas Field Examination

Location	Film Placement	Defect	Dimensions (Length x Width), mm	Average Difference in Photographic Density between Void and Base Material
1 ^a	-	None	-	-
2	A-B	Mortar Line Circumferential Vertical	2.79 x 12.7 152.4 x 12.7	0.05 0.11
2	B-C	Mortar Line Circumferential Vertical (2)	203.2 x 12.7 152.4 x 12.7 152.4 x 15.8	0.18 0.15 0.08
2	C-D	Mortar Line Circumferential	304.8 x 9.52	0.11
2	D-E	Mortar Line Circumferential Vertical	330.2 x 9.52 152.4 x 9.52	0.13 0.25
2	E-F	Mortar Line Circumferential Vertical (2)	203.2 x 7.93 177.8 x 12.7 177.8 x 15.8	0.08 0.02 0.02
2	F-G	Mortar Line Circumferential	330.2 x 9.52	0.03
2	G-H	Mortar Line Circumferential Vertical (2)	304.8 x 9.52 139.7 x 15.8 177.8 x 9.52	0.04 0.15 0.06
2	H-I	Mortar Line Vertical	152.4 x 12.7	0.02
2	I-J	Mortar Line Circumferential Vertical	165.1 x 12.7 139.7 x 15.8	0.00 0.13
2	J-K	Mortar Line Circumferential	342.9 x 9.52	0.06
2	K-L	Mortar Line Circumferential Vertical	342.9 x 6.35 152.4 x 12.7	0.15 0.15

TABLE IV. Results of Bi-Gas Field Examination (Contd.)

Location	Film Placement	Defect	Dimensions (Length x Width), mm	Average Difference in Photographic Density between Void and Base Material
2	L-M	Mortar Line Circumferential Vertical (2)	279.4 x 9.52 177.8 x 12.7 152.4 x 9.52	0.04 0.01 0.04
2	M-N	Mortar Line Circumferential Vertical	381.0 x 9.52 76.2 x 9.52	0.17 0.09
2	N-O	Mortar Line Circumferential Vertical (2)	127 x 6.35 139.7 x 15.8	0.02 0.15
2	O-P	Mortar Line Circumferential Vertical (2)	127 x 6.35 152.4 x 6.35	0.07 0.02
2	P-Q	None	-	-
2	Q-A	Mortar Line Circumferential Vertical	101.6 x 6.35 165.1 x 6.35	0.08 0.01
3	A-D	None	-	-
3	D-E	Spongy Area	177.8 x 203.2	0.20
3	E-F	Mortar Line Circumferential Vertical	330.2 x 12.7 152.4 x 9.52	0.14 0.09
3	F-G	Mortar Line Circumferential Vertical (2)	381.0 x 12.7 101.6 x 9.52 76.2 x 6.35	0.14 0.13 0.07
3	G-H	Mortar Line Vertical	82.5 x 6.35	0.07
3	H-I	Mortar Line Vertical	355.6 x 3.17	0.04
3	I-J	None	-	-

TABLE IV. Results of Bi-Gas Field Examination (Contd.)

Location	Film Placement	Defect	Dimensions (Length x Width), mm	Average Difference in Photographic Density between Void and Base Material
3	J-K	Mortar Line Vertical (2)	101.6 x 9.52 63.5 x 6.35	0.06 0.08
3	K-L	Mortar Line Vertical (2)	152.4 x 12.7 101.6 x 12.7	0.05 0.04
3	L-M	None	-	-
3	M-N	Mortar Line Vertical (2)	101.6 x 9.52 203.2 x 6.35	0.05 0.12
3	N-O	Mortar Line Vertical	127 x 6.35	0.12
3	O-P	Mortar Line Vertical	101.6 x 6.35	0.11
3	P-A	None	-	-
4	A-Q	None	-	-

^aSix radiographs, which covered 20% of the circumference, were generated at this location.

rate and rms acoustic output. Correlations were obtained with all of the transducers examined: a low-g-level accelerometer (Endevco Model 2217E), resonant acoustic-emission transducer [Acoustic Emission Technology (AET) FC-175], and broadband acoustic-emission transducer (AET FC-500-HD). The rms output is obtained using an AET Model 201 signal processor. This processor provides a true rms output, which is then measured using a Hewlett-Packard 3486 digital multimeter. The flow through the orifice is measured downstream using a Fischer and Porter ball-type flowmeter. As expected, the flow rate through the orifice is directly related to the driving pressure across the orifice. Thus, correlations can be developed in terms of either pressure or flow. The maximum permissible leak rate established by the Morgantown Energy Research Center (MERC) for their valve test facility is 10 SCFM (4.72×10^3 ml/s)/in. diam at a pressure differential of 1000 psi (6.89 MPa). The leak rate should scale in an approximately linear fashion with the pressure. In our test stand at 100 psi (0.689 MPa), the leak rates of interest should be ~ 1 SCFM (4.72×10^2 ml/s). Figure 27 shows that the leak rate for a 1/64-in. (0.40 mm) diam orifice is 0.35 SCFM (1.65×10^2 ml/s) at this pressure. Thus, this orifice appears to be a reasonable laboratory model for the type of leakage expected in practice.

The correlation developed between the rms acoustic output and the flow rate Q and driving pressure P for the low-g-level accelerometer is shown in Fig. 28. The gas in this case is dry air at room temperature (22°C). The measurements are quite repeatable. The same flow situation was also monitored using the resonant acoustic-emission transducer, and a similar correlation was obtained as shown in Fig. 29. Similar results were obtained with the broadband acoustic-emission transducer.

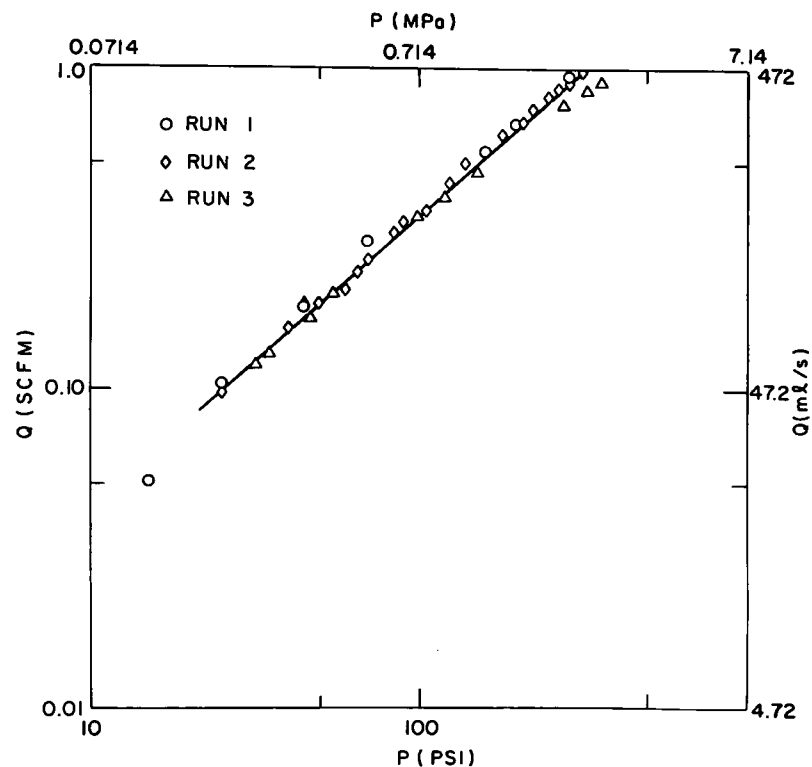


Fig. 27. Flow Rate of Dry Air at 22°C (72°F) vs Pressure Differential for a 1/64-in. (0.40 mm) Orifice. Neg. No. MSD-63436.

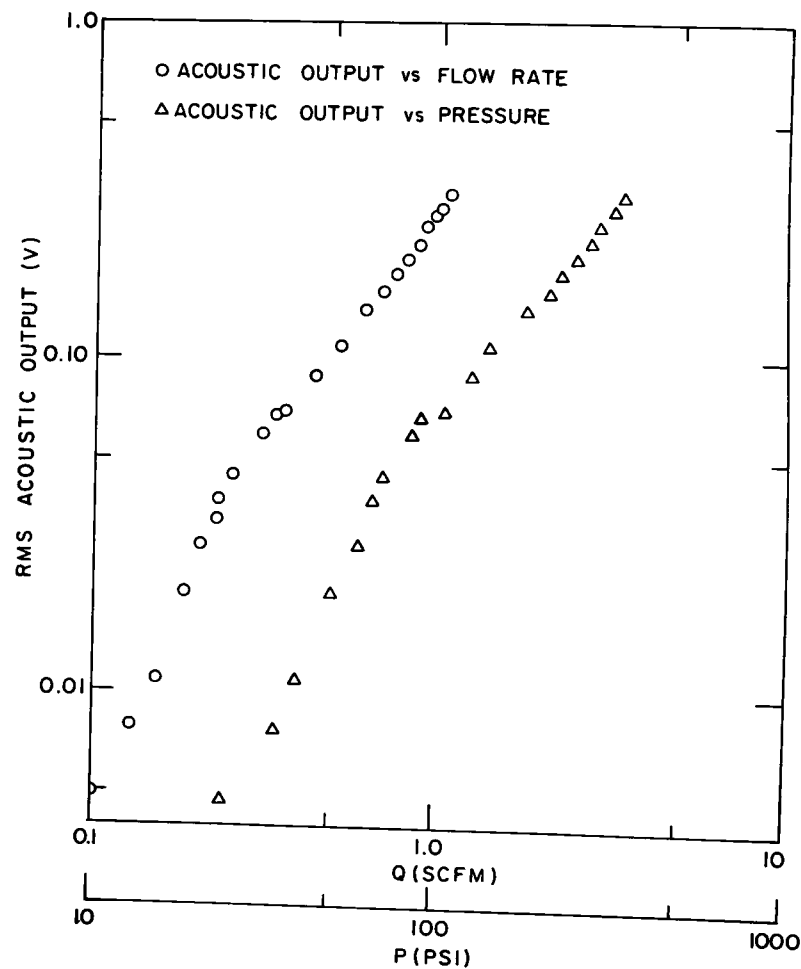


Fig. 28. Rms Acoustic Output vs Flow Rate of Dry Air at 22°C (72°F) and Pressure for a 1/64-in. (0.40 mm) Orifice Using a Low-g-level Accelerometer. Neg. No. MSD-63438.

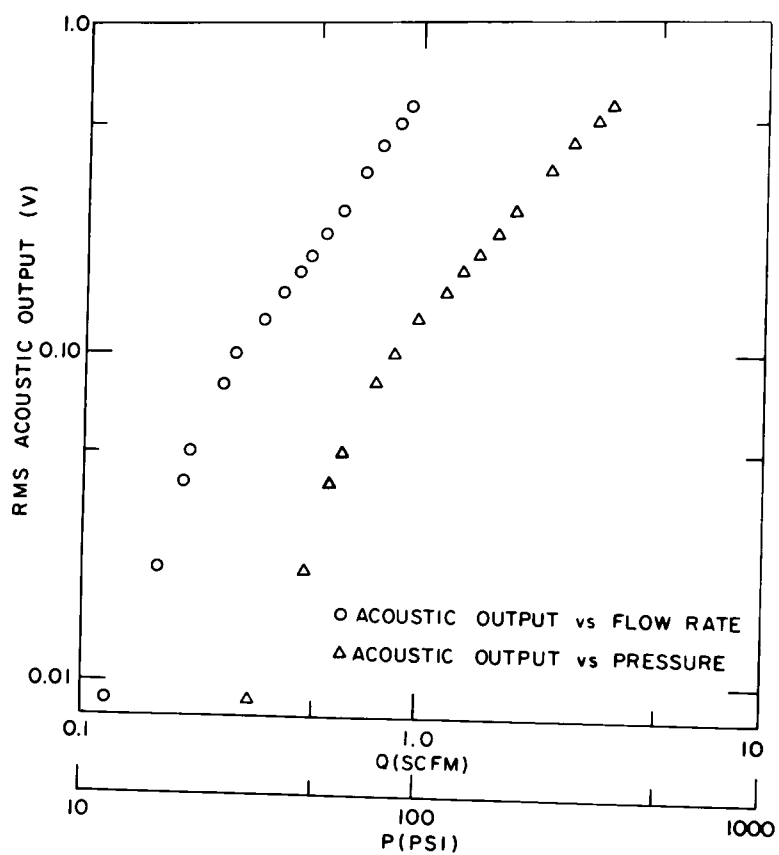


Fig. 29. Rms Acoustic Output vs Flow Rate of Dry Air at 22°C (72°F) for a 1/64-in. (0.40 mm) Orifice Using a Resonant Acoustic-emission Transducer. Neg. No. MSD-63437.

Experiments were also conducted using a 1/16-in. (1.59 mm) diam orifice. For low driving pressures the results are similar to those for the smaller orifice. However, for higher pressures a saturation effect appears, and the acoustic output is no longer monotonically related to the pressure or flow rate. Figure 30 shows results obtained for nitrogen using the broadband acoustic-emission transducer; Fig. 31 shows results obtained for carbon dioxide using the resonant acoustic-emission transducer. The saturation does not appear to be an instrumentation problem, but its origin is still unclear. Since it occurs in a flow regime of less interest for leak detection, only a modest effort will be made to find the cause for the phenomenon.

Although excellent correlations have been obtained for an orifice of fixed geometry, no common correlation has been found for orifices of different geometries. Figure 32 shows the results for the 1/64- and 1/16-in. (0.40 and 1.59 mm) orifices; for a given rms output using the resonant acoustic-emission transducer, the flow rate depends on the geometry of the orifice. Since the geometry of a leak will, of course, be unknown, the rms acoustic output is not a satisfactory acoustic parameter for quantitative leak measurement. A number of other possibilities can be explored, however. The present rms measurements are based on the acoustic power in the frequency range 125-250 kHz. (This is true even for the broadband transducer, since the contribution to the rms acoustic power from this portion of the spectrum overwhelms that from the remainder

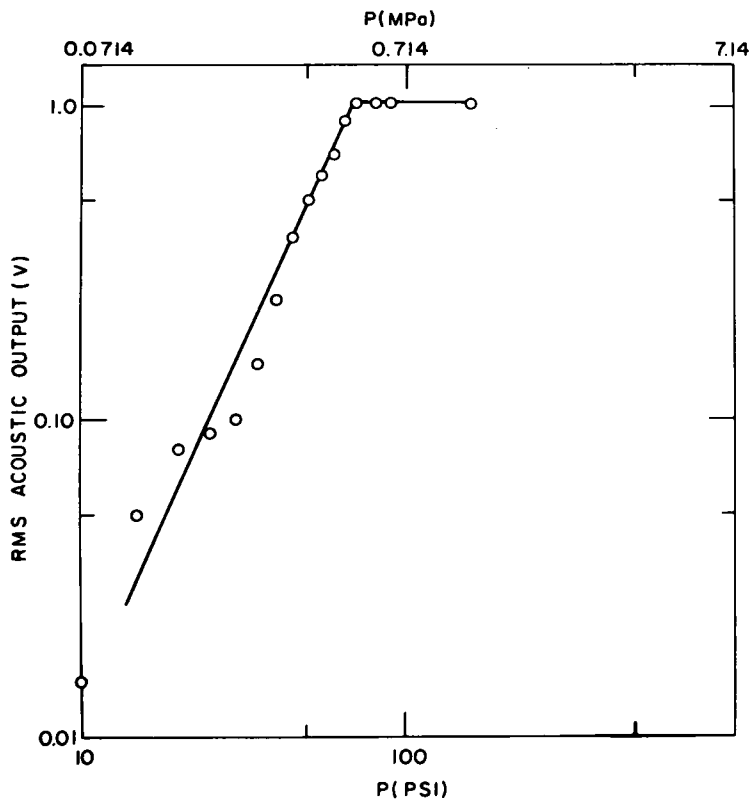


Fig. 30. Rms Acoustic Output vs Pressure for the Flow of N₂ through a 1/16-in. (1.59 mm) Orifice Using a Broadband Acoustic-emission Transducer. Neg. No. MSD-63435.

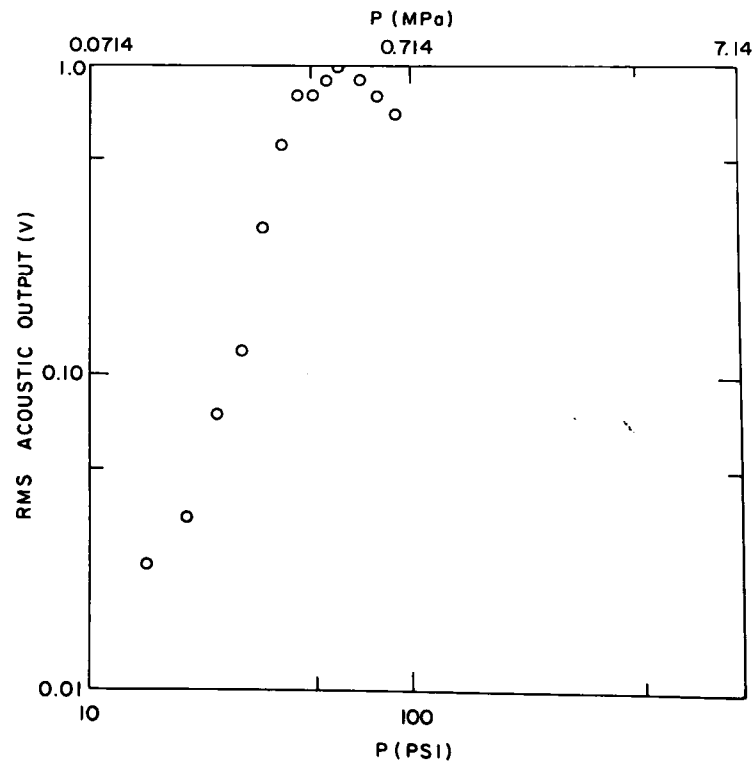


Fig. 31. Rms Acoustic Output vs Pressure for the Flow of CO₂ through a 1/16-in. (1.59 mm) Orifice Using a Resonant Acoustic-emission Transducer. Neg. No. MSD-63434.

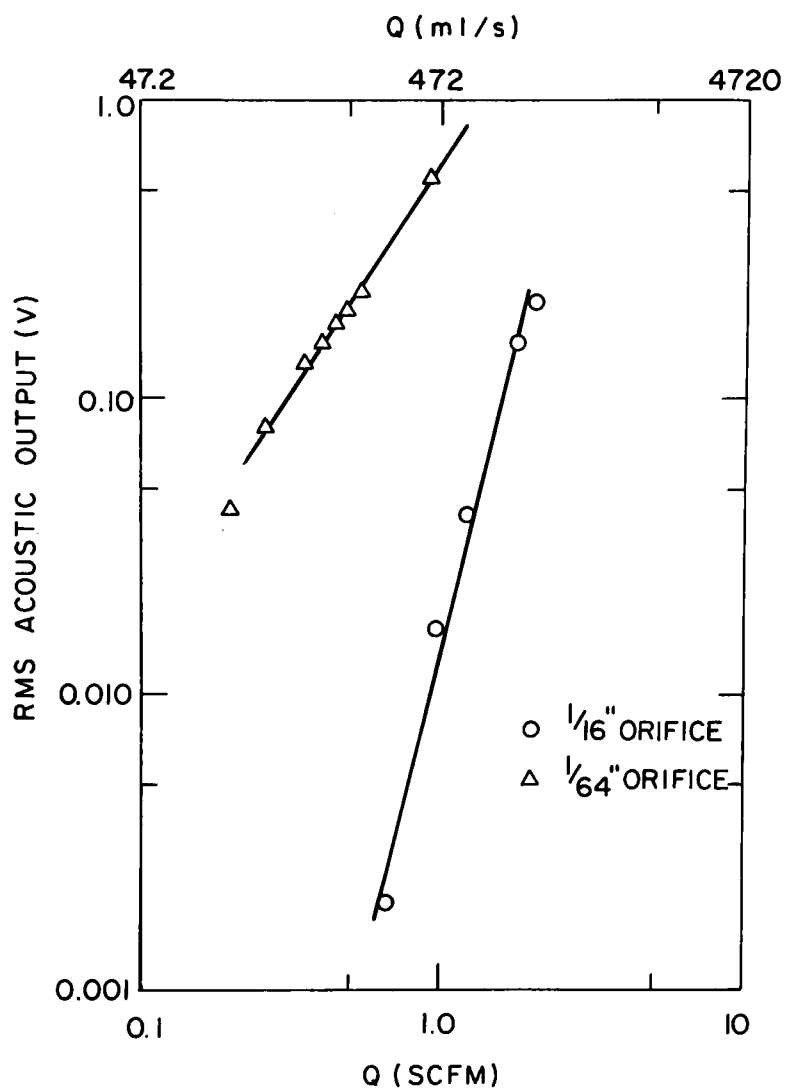


Fig. 32. Rms Acoustic Output vs Flow Rate of Dry Air through 1/16- and 1/64-in. (1.59 and 0.40 mm) Orifices Using a Resonant Acoustic-emission Transducer. Neg. No. MSD-63439.

of the spectrum.) It may be possible to obtain more satisfactory results by examining the acoustic output through a relatively narrow higher frequency window. Other signal-processing techniques may also provide the necessary results.

Cooperative efforts with MERC personnel were continued this quarter. Short-term valve instrumentation needs were discussed along with longer range needs. Field tests were planned to determine whether acoustic techniques would be suitable for their immediate needs. A joint test program was conducted with the Naval Ship Research and Development Center. A possible cooperative effort to develop a field-portable instrument was discussed.

b. Future Plans.

Arrangements have been made with personnel at the Morgantown and Synthane Pilot Plants to conduct field tests. Field measurements will be made to determine the frequency distribution of structure-borne sound in gasification plants. Once an appropriate frequency window is determined, detailed specifications for appropriate special-purpose transducers and electronics can be established. The field studies will also provide an additional opportunity to examine in more detail the problem of acoustical coupling.

The field work will be directed toward quickly developing a simple rugged instrument suitable for qualitative leak-detection work. Additional laboratory work will be performed to explore more fully the possibility of quantitative leakage measurements. Small changes of orifice diameter and length will be investigated to better understand the effect of leak geometry on acoustic output. Different types of signal processing will be examined to find acoustic parameters less sensitive to leak geometry.

Task D -- Corrosion Behavior of Materials in Coal-conversion Processes
(Principal Investigators: K. Natesan and O. K. Chopra)

The objectives of this program are to (1) develop uniaxial tensile data on four selected commercial alloys upon exposure to simulated multicomponent gas environments, (2) experimentally evaluate the high-temperature corrosion behavior of iron- and nickel-base alloys in gas environments with a wide range of oxygen, sulfur, and carbon potentials, and (3) develop a systems approach based upon available thermodynamic and kinetic information so that possible corrosion problems in different coal-conversion processes can be evaluated.

Studies on simultaneous oxidation, sulfidation, and carburization of the iron- and nickel-base alloys are being conducted in multicomponent gas mixtures that include CO , CO_2 , CH_4 , H_2 , and H_2S . Oxygen-sulfur thermochemical diagrams were used as a basis in the selection of complex gas environments for the experimental program. H_2 - H_2S and CO - CO_2 - CH_4 gas mixtures were procured, and the desired carbon, oxygen, and sulfur potentials were established by adjusting the relative flow rates of the gas mixtures. The reaction potentials of the gas mixtures in the experimental runs at 875 and 750°C are listed in Table V. Kinetic experiments were conducted in three-zone resistance-heated furnaces that contained three 35-mm OD quartz reaction tubes, which were closed at the bottom. The alloy samples (18 x 18 x 1.27-2.54 mm) were attached to a 5-mm OD thermocouple well located in the center of each reaction tube. The multicomponent gas mixture entered through a 5-mm OD quartz tube attached to the inside of the reaction tube, passed through the sample section, and exited at the top. The temperature in the vicinity of the samples was controlled to within $\sim 1^\circ\text{C}$.

TABLE V. Oxygen and Sulfur Partial Pressures (p_{O_2} and p_{S_2}) and Carbon Activities (a_C) Used in the Experimental Runs.

Mixture	875°C			750°C		
	p_{O_2} , atm	p_{S_2} , atm	a_C	p_{O_2} , atm	p_{S_2} , atm	a_C
a	8×10^{-20}	3×10^{-8}	0.226	7.8×10^{-23}	3.6×10^{-9}	0.468
b	3.9×10^{-21}	3.2×10^{-8}	0.181	1×10^{-23}	3.3×10^{-9}	0.18
c	3.1×10^{-22}	3.2×10^{-8}	0.096	2.8×10^{-24}	3.2×10^{-9}	0.096

Figures 33-35 show the oxygen-sulfur thermochemical diagrams for Types 304 and 310 stainless steel and Inconel X750 at 875°C along with the three gas environments (i.e., a, b, and c in Table V) to which the alloys were exposed. Also shown in these figures are scanning-electron-microscope photographs of the cross sections of the alloys after a 136-h exposure to the gas environments. The thermochemical diagrams show that the alloys, upon exposure to gas environment a, should preferentially form chromium oxide with sulphides in the subscale. The mixture that corresponds to b may result in either one or both phases since the chromium oxide-chromium sulfide phase boundary is not well established.

In Types 304 and 310 austenitic stainless steel, a surface layer of chromium oxide formed upon exposure to experimental gas mixture a. The thickness of the oxide layer was 10 μm . In the interior of the specimens, a few chromium sulfide particles were observed. In general, the oxide layers were adherent to the alloy surface. Upon exposure to gas environment c, the steels showed predominantly sulfides in the scale region. The sulfide layer consisted of alternate layers of chromium and iron sulfide as shown in the high-magnification photographs of the scale in Figs. 33 and 34. The thickness of the scale and sulfidized regions of the samples corresponded to 0.40 and 0.35 mm, respectively. The nickel content in these steels (10-20 wt%) and the sulfur potentials employed in the experiments were insufficient to cause formation of nickel sulfide. The higher chromium content in Type 310 stainless steel (25 wt%, compared with 19 wt% in Type 304 stainless steel) only slightly lowers the sulfur potential necessary to form chromium sulfide when compared with Type 304 steel. As the chromium sulfide phase forms in these steels, a depletion of chromium in the matrix occurs; under such conditions, the sulfur potential necessary to form iron sulfide in the alloy may

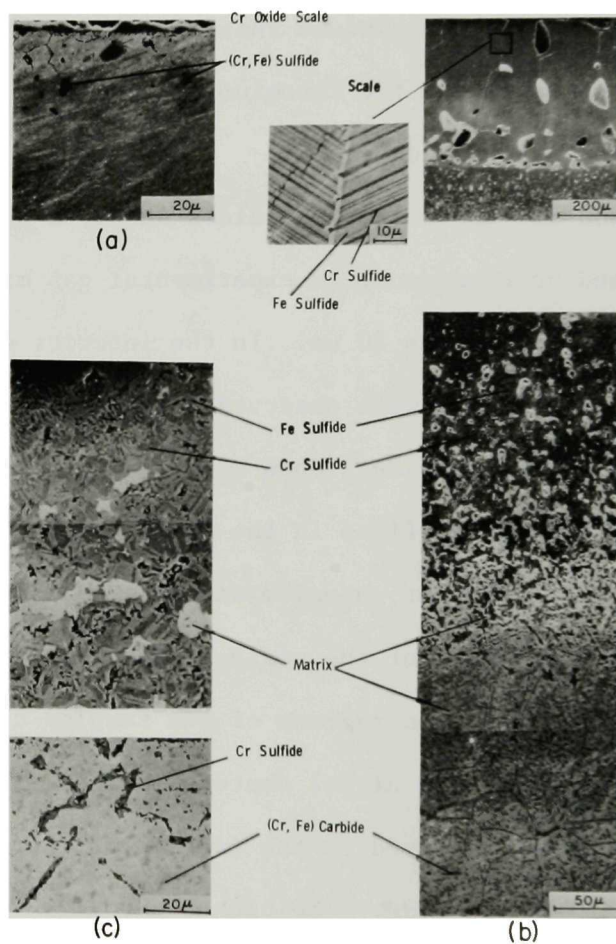
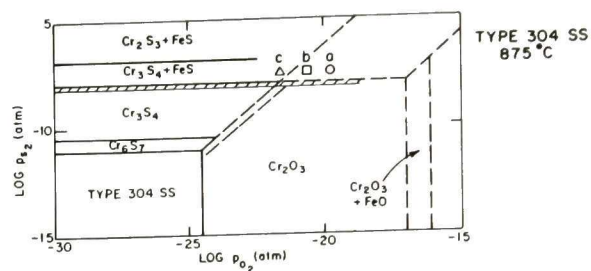


Fig. 33. Scanning-electron Micrographs of Type 304 Stainless Steel after a 136-h Exposure at 875°C to Gas Environments Identified as a, b, and c in the Thermochemical Diagram. Neg. No. ANL-306-76-176.

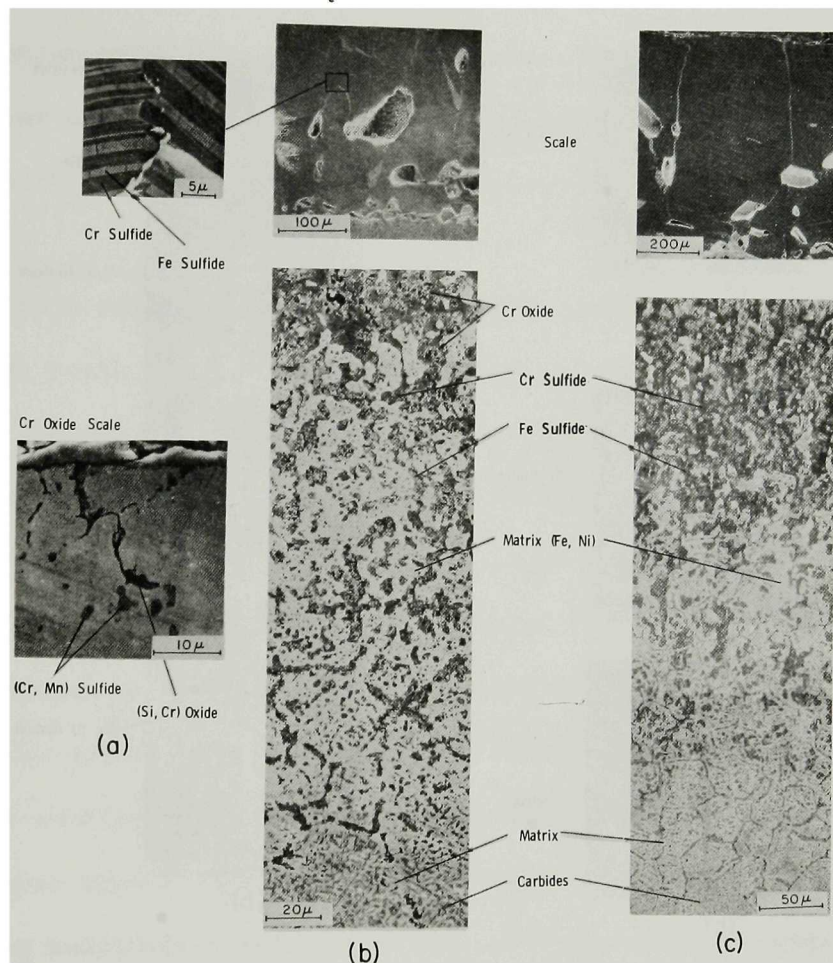
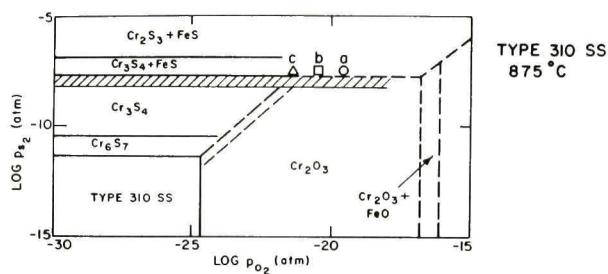


Fig. 34. Scanning-electron Micrographs of Type 310 Stainless Steel after a 136-h Exposure at 875°C to Gas Environments Identified as a, b, and c in the Thermochemical Diagram. Neg. No. ANL-306-76-178.

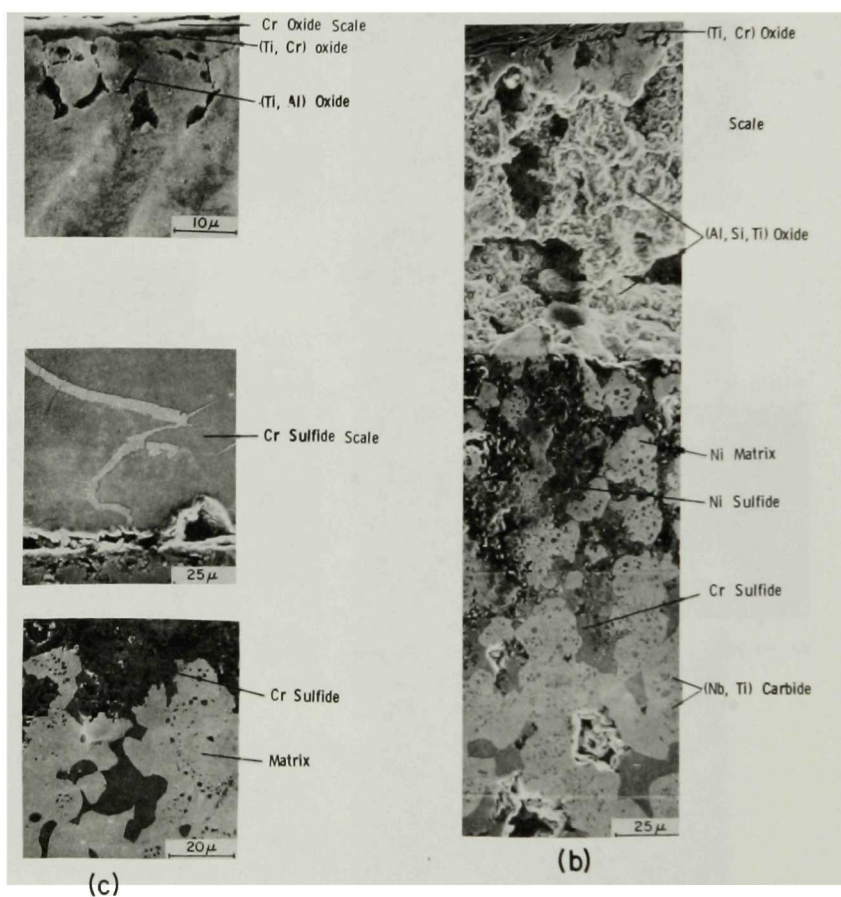
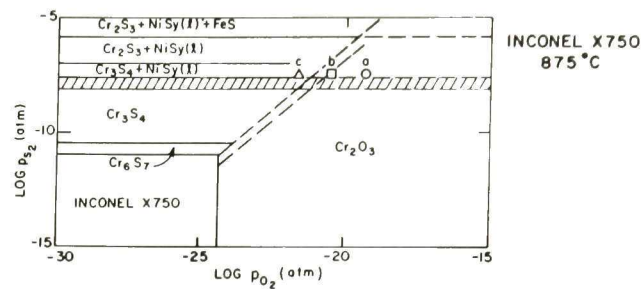


Fig. 35. Scanning-electron Micrographs of Inconel X750 after a 136-h Exposure at 875°C to Gas Environments Identified as a, b, and c in the Thermochemical Diagram. Neg. No. ANL-306-76-177.

approach a value that corresponds to iron-iron sulfide equilibrium. This is indicated by the lower line of the hatched area in Figs. 33 and 34, and the upper line of the hatched area corresponds to iron sulfide formation in the original Fe-Cr-Ni alloy. The micrographs of the alloys exposed to gas environment b show the formation of oxides and sulfides, and the alloy behavior in terms of depth of penetration of the reaction zone is essentially similar to that for the materials exposed to gas mixture c. The results also show that the chromium oxide/chromium sulfide phase boundary must be evaluated more accurately over a range of temperatures to establish the critical oxygen pressure below which the alloy will exhibit sulfidation rather than protective oxidation.

Inconel X750 alloy, which contains 73 wt% nickel, showed a protective (Cr, Ti) oxide scale upon exposure to mixture a. As the oxygen potential decreased to that of mixture b, the alloy exhibited a discontinuous, porous (Cr, Ti) oxide scale. As a result, the sulfur potential established at the scale/metal interface was almost the same as in the gas phase. Under such conditions the specimen exhibited chromium sulfide and local pockets of nickel sulfide, which is liquid at the exposure temperature. In the interior of the sample, where the sulfur potential drops below that for nickel-nickel sulfide equilibrium, only chromium sulfides were observed. The samples also showed significant precipitates of (Nb, Ti) carbides in advance of the sulfidation-reaction front. The specimens exposed to gas environment c had a scale of chromium sulfide with some particles of titanium oxide that formed by internal oxidation. The thickness of the chromium sulfide layer formed in this specimen is significantly larger than that of the oxide layer formed in environment a; however, the sulfide layer is adherent enough that a sulfur gradient is established between

the gas phase and the interior of the specimen. Since no nickel sulfide was observed in the interior of the specimen, the sulfur potential at the advancing chromium sulfide front must be lower than that for nickel-nickel sulfide equilibrium.

Inconel 671 alloy specimens exposed at 875°C to gas environments a, b, and c showed protective chromium oxide in a, chromium sulfide in c, and a mixture of both oxide and sulfide in b. No evidence of nickel sulfide occurred in the exposed specimens in any of the three environments. On the other hand, specimens of the same alloy exposed at 750°C to the gas mixtures showed no oxide protection. Figure 36 shows the oxygen-sulfur thermochemical diagram for Inconel 671 at 750°C along with scanning-electron-microscope photographs of the cross sections of specimens exposed for 25 h. The specimens exhibited a scale that contained predominantly chromium sulfide and liquid nickel sulfide. The liquid sulfide that formed at the exposure temperature appears to have squeezed out from the interior of the scale and sample onto the scale surface, as shown in Fig. 36.

The results obtained thus far indicate that the corrosion behavior of commercial iron- and nickel-base alloys in multicomponent gas environments is complex and that fundamental processes such as oxidation, sulfidation, and carburization can occur simultaneously with different advancing reaction fronts. The results also indicate that thermochemical diagrams can be used to analyze the material behavior in complex

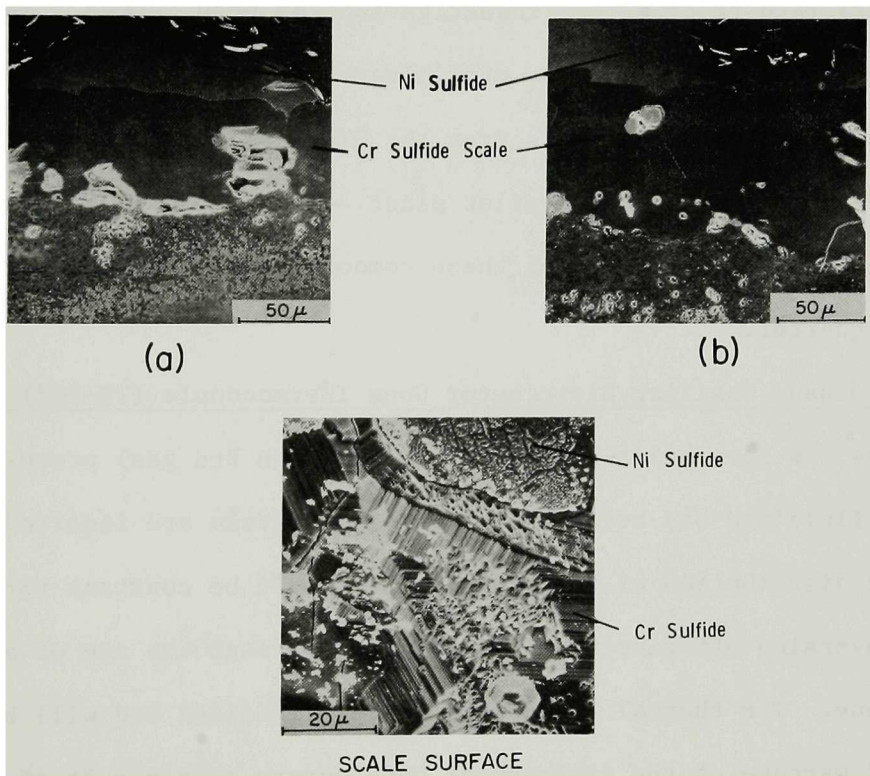
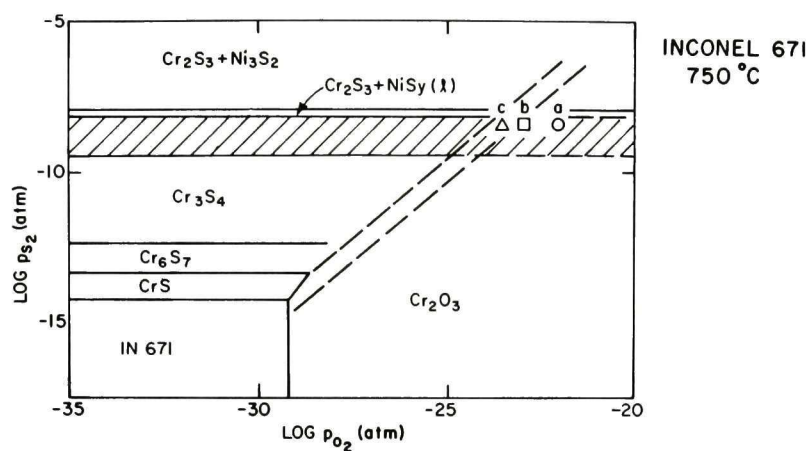


Fig. 36. Scanning-electron Micrographs of Inconel 671 after a 25-h Exposure at 750°C to Gas Environments Identified as a and b in the Thermochemical Diagram. Neg. No. ANL-306-76-175.

environments and establish the applicability of a given alloy in specific environments. Additional experiments are being conducted to evaluate the corrosion behavior of these materials as a function of time, temperature, and gas composition.

Task F -- Component Performance and Failure Analysis (Principal Investigators: S. Danyluk, G. M. Dragel, W. J. Shack, and W. A. Ellingson)

The principal activity during this quarter involved a critical examination of the Synthane failed thermocouple sheaths used in the temperature-sensing system of the gasifier distributor cone. A final report of the results from this investigation has been issued, and a summary is provided below. Also, preliminary field data have been collected on seven failed components from the HYGAS pilot plant, one from MERC, and one from the Synthane pilot plant. These components are listed in Table VI. Failure analysis of these components will be conducted in the coming quarter.

1. Synthane Gasifier Distributor Cone Thermocouple (TE-268) Failures

The Synthane pilot-plant conversion (high Btu gas) process utilizes a fluidized bed below which oxygen and steam are inserted. The temperature distribution of the fluidized bed must be constant for optimal process conversion efficiency and is obtained through the use of a distributor cone. The thermal uniformity of the fluidized bed will be affected if warpage of the distributor cone occurs as a result of overheating. A detailed schematic of the gasifier, including the distributor cone, is shown in Fig. 37. The temperature of the cone is continuously monitored by thermocouples, which are enclosed in sheaths that have one end welded to the cone surface. These sheaths failed near the inlet in

TABLE VI. Failed Components to be Analyzed in the Coming Quarter

Facility	Component
HYGAS Pilot Plant	(1) Char Carrier Line
	(2) 1/4-in. Nitrogen Purge Line (339 Line)
	(3) Flange (322 Line)
	(4) Type 316 SS Nitrogen Purge Line
	(5) Type 316 SS High-pressure Water Elbow
	(6) Thermocouple Protection Tube
	(7) Bellows
Morgantown Energy Research Center	(8) Stirrer from the High-pressure Gas Producer
Synthane Pilot Plant	(9) Valve Stem from an EBV Ball Valve

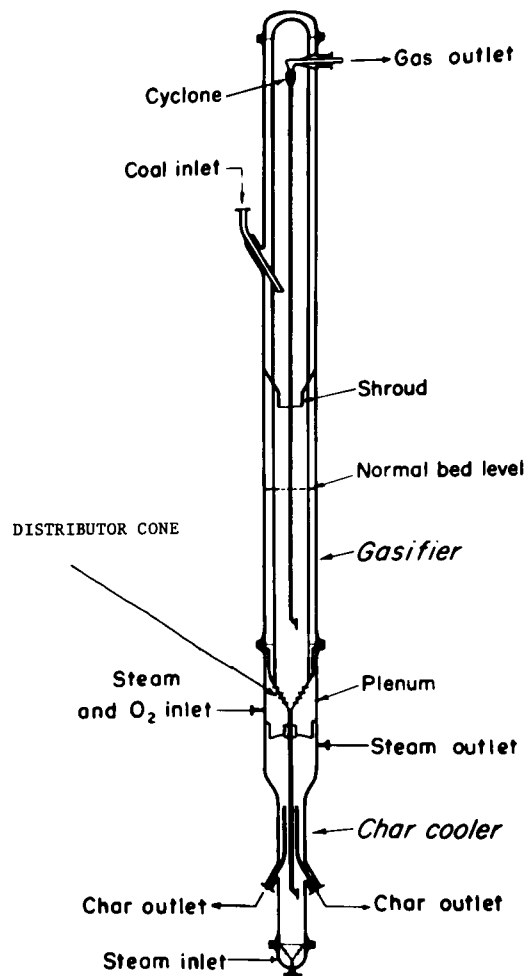


Figure 2 — SYNTHANE gasifier

Fig. 37. Schematic of Synthane Gasifier.
Neg. No. MSD-63545.

the plenum region of the gasifier by rupture of the tube walls and exposure of the thermocouple wire and magnesium oxide insulating material to the gasifier environment. The failures are related to sulfur-associated corrosion and plastic deformation and tearing in part due to the expansion of the magnesium oxide. The thermocouple failures impair the operation of the pilot plant.

Twelve thermocouple sheaths (TE-268) are brazed onto a carbon steel flange. Two of these flanges are mounted, one on either side of the distributor cone. The sheath material is Incoloy 800, and a magnesium oxide powder insulates the Chromel/Alumel thermocouples. The sheaths were exposed to the gasifier environment, which is nominally steam and oxygen [4 MPa (600 psig) and 393°C (650°F)], for a total of ~15 h. The sheaths were also exposed to flue gases, which are generated by a start-up burner that preheats the gasifier. A fuel oil (Number 2) that contains ~0.4 wt% sulfur is used by the start-up burner.

The failures are believed to have occurred in two stages. Corrosion initiated at the OD surface of the sheath material in surface cracks or pits. The corrosion cracks are randomly oriented. Where the cracks penetrated to the ID surface and exposed the magnesium oxide to the steam environment, they were opened further by formation of $\text{Mg}(\text{OH})_2$, which possesses a molecular volume double that of MgO . The sheath material plastically deformed and ruptured along the tube axis as the insulating material expanded. It is believed that a corrosive environment, off-process temperatures, sheath fabrication factors, and possible cold work of the thermocouple sheaths contributed to the failures. This hypothesis is predicted on the following facts:

- a) A high sulfur content was found in the corrosion scale and precipitates wedged in cracks on the fracture surface.
- b) The surfaces of failed tubing and tubing that had not been in service contain shallow cracks and pits.
- c) High microhardness values were recorded from the failed regions of the sheath.

Analysis indicates that residual H_2O in the MgO alone could not have caused the failures.

The following were recommended to Synthane personnel:

- a) Careful control of the sheath fabrication is advisable. The RDT Standard (Specification #C7-6T) for metal-sheath, ceramic-insulated thermocouples may be used as a guide.
- b) A higher chromium stainless steel (Type 310) should alleviate the sulfidation problem.
- c) Since the flue gases in the start-up burner contain sulfur (~ 0.4 wt%), using propane as a fuel should considerably reduce the sulfur contamination.
- d) Careful handling of the tubes and annealing prior to installation should eliminate the cold work.

References

1. Materials Science Division Coal Technology Seventh Quarterly Report, April-June, 1976, Argonne National Laboratory, ANL-76-111.
2. Materials Science Division Coal Technology Sixth Quarterly Report, January-March, 1976, Argonne National Laboratory, ANL-76-60.
3. Materials Science Division Coal Technology Fifth Quarterly Report, October-December, 1975, Argonne National Laboratory, ANL-76-22.
4. Acoustic Emission from Polycrystalline Ceramics, SC531.7FR Final Report Submitted to the Department of the Navy, Naval Air Systems Command, Washington, D.C. by the North American Rockwell Science Center, December 1972.

Distribution of ANL-76-111

Internal:

E. G. Pewitt
A. D. Tevebaugh
B. R. T. Frost
R. W. Weeks (6)
M. F. Adams
O. K. Chopra
S. Danyluk
D. R. Diercks
W. A. Ellingson (6)
J. Fischer

A. A. Jonke
T. F. Kassner
C. R. Kennedy
A. B. Krisciunas
K. Natesan
J. L. Nivens
R. B. Poeppel
W. J. Shack
ANL Contract Copy
ANL Libraries (5)
TIS Files (6)

External:

ERDA-TIC, for distribution per UC-90h (212)
Manager, ERDA-CH
Chief, Chicago Patent Group
President, Argonne Universities Association
Materials Science Division Review Committee:
R. W. Balluffi, Cornell Univ.
S. Doniach, Stanford Univ.
H. L. Falkenberry, Tennessee Valley Authority
C. Laird, Univ. Pennsylvania
D. Lazarus, Univ. Illinois
M. T. Simnad, Gulf General Atomic
A. R. C. Westwood, Martin Marietta Laboratories
V. F. Zackay, Univ. California, Berkeley
R. R. Adams, Battelle Columbus Laboratories
W. G. Bair, Inst. of Gas Technology
W. Bakker, USERDA/FE
S. Carson, CE Lummus Co., Bruceton, Pa.
A. Conn, Amoco Oil Co., Naperville, Ill.
W. C. Corder, Battelle Columbus Laboratories
M. Crowley, Standard Oil of Indiana, Naperville, Ill.
J. Flagg, Universal Oil Products Co., Des Plaines, Ill.
E. Fox, Stearns-Roger Corp., Homer City, Pa.
H. E. Frankel, USERDA/FE
D. Glaser, Stearns Roger Corp., Denver
H. Heystek, Tuscaloosa Metallurgy Research Center, University, Ala.
V. Hill, IIT Research Inst.
D. Hull, Phillips Petroleum Co., Homer City, Pa.
H. Leavenworth, U. S. Bureau of Mines, Washington
R. Lewis, Synthane Pilot Plant, USERDA/FE, Pittsburgh
G. Long, Northern Illinois Gas Co., Aurora
R. M. Lundberg, Commonwealth Edison Co., Chicago
A. L. Plumley, Combustion Engineering Power Systems, Windsor
A. Schaeffer, Metals Properties Council, New York
S. J. Schneider, National Bureau of Standards
J. R. Schorr, Battelle Columbus Laboratories
J. Stevenson, Rolla Metallurgy Research Center
J. Sudbury, Consolidated Coal Co., Library, Pa.

C. Whitten, Peabody Coal Co., Columbia, Tenn.
F. Woods, Albany Metallurgy Research Center
A. V. Levey, Lawrence Berkeley Laboratory
J. M. O'Donnell, The Lummus Co., Bloomfield, N. J.
R. I. Jaffee, Electric Power Research Institute
D. L. Keairns, Westinghouse Research Labs.
S. M. Gaitonde, Commonwealth Edison Co., Maywood, Ill.
E. M. Anderson, The Babcock & Wilcox Company

ARGONNE NATIONAL LAB WEST



3 4444 00024145 5

X